

1 Reply to Anonymous Referee #1 from 21 Oct 2017

2 *Note: Author responses are in plain text following the original referee comment shown in italicized text.*

3 *The figures, in particular the captions need some work. My opinion is that figures and captions should be stand*
4 *alone, such that a reader should be able to understand what each figure is without reading the text. In some cases*
5 *adding a key or a description of symbols in the figure caption would achieve this goal. For example, Figure 3 has no*
6 *key for the classified image.*

7 We have added a classification key to Figure 3. Thank you for the suggestion – we have also incorporated
8 edits throughout to make image captions more complete and descriptive.

9 *Line 50. Missing a reference to Fetterer and Untersteiner (1998).*

10 We have included this reference as well as one to Arntsen et al. 2015.

11 *Line 63. When discussing alternative classification methods, it would be good to enumerate those methods applied*
12 *to classification of sea ice. Furthermore, the authors give maximum likelihood classification as an example or an*
13 *unsupervised algorithm. Maximum likelihood can be a supervised algorithm.*

14 Each reference on line 63 details a classification method applied to sea ice. We have edited line 98 to
15 indicate that those references refer to a method applied to image processing generally, and not specifically to
16 the classification of sea ice.

17 It is true that maximum likelihood classifiers can be supervised in some cases - we have revised this
18 discussion of unsupervised classification algorithms to be more precise.

19 *Section 4.1. In the analysis of seasonal evolution of surface characteristics, my guess is that the field of view does*
20 *not contain the same ice. The authors should make this clear or state why they think it is the same floe/ice. How fast*
21 *is the ice likely to be moving at this location?*

22 You are correct – the ice seen at this location is not a single floe. This explains the sudden increase and
23 then subsequent decrease in open water fraction in late June, as well as the completely ice-free water by
24 August. We have included the following sentence in Section 4.2 to clarify that we are looking at Eulerian
25 rather than Lagrangian view: “The site is Eulerian; it observes a single location in space rather than follow
26 a single ice floe through its lifecycle as it drifts”.

27 *Line 433. I disagree with the statement that misclassification means that the algorithm fails to replicate human*
28 *decision making. That might be the goal but one that is impossible to reach. To my mind, misclassification indicates*
29 *that the algorithm doesn't give the same answer as a human would.*

30 We agree that we are not replicating the decision-making process, but rather the end result. We have
31 revised this section to clarify our definition of misclassification. Line 474 was changed to: “The algorithm
32 either assigned the same classification as a human would have, or it did not”, and line 478 has been
33 rewritten to: “The first type of internal error is misclassification error, where the image classification
34 algorithm fails to assign the same classification that a human expert would choose”.

35 *Line 531. This analysis is interesting but does it apply to the image used or to all images in general. How might the*
36 *result change through time or with season?*

37 This analysis applies specifically to the image used, though there is nothing particularly unique about the
38 image analyzed. We believe the results are applicable to all images in general, but a complete
39 demonstration of that is better suited to its own study, and we suggest future work to expand this analysis to
40 a general rule. The statistical methods that we use here should be independent of the seasonality of ice (so
41 long as the metric you are investigating can be captured by the image scale, e.g. this works for melt pond
42 fraction and not for ice fraction). At the core, we are just using a sample of some size as a means to
43 estimate a population statistic.

44 We have added line 598 to detail this in the manuscript: “The statistical approach for determining image
45 statistics should not depend on the seasonality of the image nor the type of image used so long as the total
46 area observed is sufficiently greater than the variability in the surface feature being investigated.”

47 *Line 558. The Central limit Theorem is a mathematical theorem complete with proof. I wouldn't say that it can be*
48 *tested. What you are doing here is evaluating if you can predict the regional/image mean from a set of smaller*
49 *samples/local means. One framework to evaluate this is hypothesis testing in which you pose the hypothesis that N*
50 *sample means can predict/estimate the regional mean. This test applies the Central Limit Theorem but does not test*
51 *it. This section needs to be reworked.*

52 *Line 559. The standard definition of the Central Limit Theorem is that independent variables can be added and*
53 *normalized by $(X - \mu)/(\sigma/\sqrt{n})$ to yield a normal distribution $N(0,1)$. Where X is the sample mean, mu*
54 *population mean and sigma population standard deviation.*

55 These are good points. We have significantly revised this section. The takeaway message remains largely
56 the same as in the original version, but both the text and methodology has been improved for new version.
57 Instead of applying the Central Limit Theorem directly, we instead analyze the sample size required to
58 estimate the regional mean, and address the difference in measuring from spatially correlated samples
59 versus randomly selected samples.

60 *Figures: Check figure numbering*

61 Thanks for catching this – we have fixed the figure numbering issue.

62 *Figure 13. The cyan rectangle over the black dots make the dots look green (at least on my screen). The labels in the*
63 *key need to match the description in the text. If some of the information is not discussed, I suggest removing it from*
64 *the figure.*

65 We have fixed the coloration issue with the mean dots.

66

1 Reply to Anonymous Referee #2 from 21 Oct 2017

2 *Note: Author responses are in plain text following the original referee comment shown in italicized text.*

3 *Line 50. I suggest adding Fetterer and Untersteiner (1998) and Arntsen et al. (2015) to the reference list.*

4 We have added both references to this section. Although the Arntsen et al. 2015 paper uses the method
5 presented in Miao et al. 2015.

6 *Line 66. This isn't quite right. Several previous works have demonstrated surface feature retrievals from high-
7 resolution imagery throughout the seasonal evolution of ice surface conditions.*

8 We have reviewed a large number of previous works detailing the classification of high resolution optical
9 imagery of sea ice (e.g. Arntsen et al., 2015; Fetterer and Untersteiner, 1998; Inoue et al., 2008; Kwok,
10 2014; Lu et al., 2010; Miao et al., 2015; Perovich et al., 2002b; Renner et al., 2014; Webster et al., 2015),
11 and have not come across any that are demonstrated on a complete seasonal melt cycle. To the best of our
12 knowledge no such work exists. We will gladly incorporate further information into this section if the
13 reviewer can point us to the references they are referring to.

14 *Lines 136+. How does the algorithm differ from that in Miao et al? Please describe any differences.*

15 While this algorithm is inspired by the work of Miao et al. 2015 to use image segmentation followed by
16 classification with a random forest algorithm, the implementation of that workflow is quite different. To
17 convey this, we have added line 132: "Our implementation of the segmentation and classification, however,
18 were custom-built using well known image processing tools (Pedregosa et al., 2011, van der Walt et al.,
19 2014) in an open source format".

20
21 The algorithm presented by Miao et al. (2015) uses the ENVI GIS software package. As such, there are some
22 specifics that remain proprietary to ENVI. Where we know how the Miao et al. algorithm behaves, we have
23 stated the similarities and differences. We use a custom-built segmentation technique (section 3.2) that is
24 different than the Miao et al. method. In the random forest machine learning technique, we use some attributes
25 that were developed by Miao et al. (2015) (attributed in line 267 and 303), as well as attributes new to our
26 method (lines 302-313).
27

28 *Line 236. Does this melt pond definition include or exclude melt ponds that are melted through? Relative to previous
29 works, is it typical to include submerged ice in the melt pond class or is it unique to this approach?*

30 Our melt pond definition, which is provided in lines 239-248. excludes the area of melt ponds that has
31 melted through completely (see Figure 5). Our approach to the surface classifications was to consider
32 primarily shortwave optical properties. Submerged ice and melt ponds have similar optical properties and
33 impact the solar energy balance in the same way. Thus it makes sense to group them into a single category.
34 Previous works have taken both approaches. Miao et al. (2015), for example, presented a method for
35 distinguishing general submerged ice from contained melt ponds by analyzing their proximity to open
36 water. However, separating these classes is not necessary for all applications. Spectral unmixing
37 algorithms, such as those presented by Rosel et al. 2012, to determine melt pond fraction on a larger scale
38 consider only aggregate optical properties, and melt pond fraction would necessarily include the general
39 submerged ice category as well.

40 *Line 241. Submerged ice isn't a type of melt pond. Please clarify this point. It would be helpful to comment on the
41 effects of submerged ice on melt pond statistics of area and geometry, especially for scenes of advanced melt in the
42 marginal ice zone.*

43 *Lines 361+. It would be helpful to explicitly include submerged ice in the melt pond class throughout the text and
44 figures. For example, instead of "Melt pond," please state "Melt pond and submerged ice" or "Melt pond +
45 submerged ice."*

46 To be more clear on our definition, we have changed this category to be "melt pond and submerged ice"
47 throughout the figures and text.

48 Our hope is to spur community discussion with these surface type definitions, and so we have presented
49 what we feel is the most widely applicable way to standardize 'ponded ice'. We acknowledge in line 236
50 that there are different opinions. We found that many experts in the sea ice community have subtly
51 different definitions of the surface types, even beyond the distinction being made here. (as we discovered
52 when producing the data for Figure 4.) From a shortwave optical stand point, submerged ice and melt
53 ponds are functionally the same, and since radiative balance is a primary reason to study ponds, we argue in
54 line 244-245 that it makes sense to group them as a single category. For a study concerned with pond
55 geometry this is obviously not the case, and there are methods (such as those discussed in Miao et al. 2015)
56 to separate general submerged ice from melt ponds. These could easily be applied to our output by an
57 interested user.

58 *Line 245. Would this criterion also include sea ice darkened by sediment and algae during the melt season?*

59 Yes, though we have not seen either of these features in the images we processed for this paper.

60 *Lines 252 and 307. Please provide more details on the shadow detection step for panchromatic and multispectral
61 imagery. Does it differ from previous works?*

62 We did not use the shadow category for multispectral imagery. There is not a separate step for shadow
63 detection, per se, rather an additional training category for the machine learning algorithm. We have edited
64 the discussion of the shadow category in section 3.3.2 to reflect that we are not presenting shadows as a
65 classification category. We have also added lines 258-261 to illustrate the differences to previous
66 approaches to handling shadows.

67 This step does differ from previous work. In Webster et al. (2015), for example, ridge shadows are directly
68 masked and set to the maximum pixel values. Our approach also differs from that in Miao et al. (2015), as
69 our shadow class is not an independent classification in the output and it is only used for images prior to
70 melt onset. Miao et al. (2016) details a more sophisticated ridge and shadow detection scheme

71 *Line 290. Please describe how image dates are used in the classification scheme.*

72 We have edited lines 296-300 to clarify how image dates are used for classification. The image acquisition
73 dates are an attribute that the random forest can use to make a prediction. Image date is a simple means of
74 estimating melt state, which improves the ability of the classifier to correctly predict surface conditions.

75 *Lines 305/491. How does this step distinguish a neighboring ridge from snow-covered ice? It's not clear, does the
76 algorithm identify ridges as a separate class?*

77 Line 491 incorrectly implied that we are detecting ridges directly. We've edited line 491 to clear up this
78 point. While we have methods for indirect detection of ridges (i.e. their shadows – see revised lines 258-
79 261) we do not distinguish ridges from snow covered ice. We have reworked lines 309-318 to illustrate that
80 bright ridge pixels are an example of the benefit of looking at object neighbors, and not a method for
81 creating a ridge class.

82 *Line 310. Here and elsewhere, trade-offs in computational expenses are mentioned. It would be helpful to give a
83 ballpark estimate of the computational expense if possible, e.g., is it $O(N)$ or $O(N^2)$?*

84 The algorithm is roughly $O(N)$, but it is difficult to quantify the computational expense in big-O terms for
85 this application. High resolution satellite images are quite large, and can easily have millions of image
86 objects. Therefore, any small increase in the time required to evaluate each image object (such as a more
87 complex neighbor analysis) dramatically increases the total processing time.

88 We have edited lines 197, 274 to refine our meaning behind 'computational expense'.

89 *Line 313. It's surprising that the Literal Image Derived Products from the Global Fiducials Library have been
90 excluded from this analysis, as these publicly available images have been the data source for several analyses of
91 high-resolution sea ice imagery (Arntsen, Fetterer, Kwok, Webster). Do the authors anticipate that users will find
92 the algorithm suitable for processing this imagery given its radiometric inconsistencies? Why or why not?*

93 We do not anticipate any issues with the NTM imagery from the Global Fiducials Library, and 1m
94 resolution is high enough to get good results (see figures 11 and 12). From an image processing standpoint,
95 the NTM imagery is very similar to panchromatic WorldView imagery, and we therefore do not believe

96 processing the NTM imagery would change the discussions of this paper. In unpublished work Arntsen has
97 tested this algorithm on the NTM imagery with success.

98 We have added line 151: “The imagery sources chosen for this analysis were selected to be representative
99 of the variation that exists in optical imagery of sea ice, but there is an abundance of image data that can be
100 processed with this technique.”

101 *Line 319. Are the different results between experienced and inexperienced users a matter of definition? For
102 example, how do experienced and inexperienced users classify submerged ice near floe edges?*

103 The experience and inexperienced users had the same classification definitions in front of them as they
104 worked their way through the training sets. Though some users might have had different opinions of the
105 surface types on their own, the lack of standard definition is not the reason for disagreement. The
106 definitions of the ice types, including for example submerged ice, were set in advance and provided to all
107 users. The differences arise from the user’s ability to interpret the definitions and apply them. We have
108 added a sentence in the paper clarifying this point (line 329). As we established the definition of melt pond
109 to include submerged ice on the edge of a floe ahead of time, users were consistent in their classification of
110 these categories.

111 *Lines 406+. Is this an Eulerian or Lagrangian site? How do the authors distinguish changes due to spatial
112 heterogeneity from seasonal melt progression?*

113 *Line 786/Figure 10. Please state whether this site was Eulerian or Lagrangian in the caption.*

114 The site is Eulerian. We have clarified this in the relevant figure captions and added line 505: “The site is
115 Eulerian; it observes a single location in space and does not follow a single ice floe through its lifecycle as
116 it drifts”.

117 *Lines 508+. For the aggregate-scale analysis, what type of ice was present in the analyzed scenes? How might the
118 results change based on the presence of different sea ice types?*

119 The images used in the aggregate scale analysis contained primarily first year ice in various stages of melt,
120 and we have noted this in line 522. We have noted in the manuscript in lines 585/591 that this method
121 applies only to melt pond fraction, as we discovered that the images were not large enough to accurately
122 capture ice fraction. Within the melt pond fraction category, we do not believe a different ice type would
123 substantially change the results (lines 594-596), as this analysis is at its core a statistical problem (how to
124 estimate a population based on a sample).

125 *Lines 760/Figure 4 & 779/Figure 8. I suggest presenting the pixel counts as percentages of the total pixels evaluated
126 and providing the total pixel count in the caption for ease of reading.*

127 That is a good suggestion. We have added that information to the figure.

128 *Line 782/Figure 9. In the caption or text, please provide the average scene size.*

129 Another good suggestion, which we have also added to the figure caption.

130 *Line 791/Figure 11. I suggest adding the resolution size as a secondary x-axis on the top of the plots for ease of
131 reading.*

132 We have changed the x-axis to be in units of resolution in meters. The axis is still on a log scale, but as you
133 suggested, it is much easier to read in this format.

134 *Line 52. Morphology seems like the wrong word here.*

135 Changed ‘morphology of surface conditions’ to ‘morphology of surface features’. The morphology of a
136 feature is its structure or form, and here we are discussing the difficulty of lower resolution optical sensors
137 in directly observing the structure of surface features

1 Reply to Anonymous Referee #3 from 04 Nov 2017

2 *Note: Author responses are in plain text following the original referee comment shown in italicized text.*

3 *Please note that there is a previous effort to realize an open source package for sea ice feature detection: Sea Ice*
4 *Imagery Classification with Machine Learning and High-Performance Computing, XSEDE 2016 Polar Compute*
5 *Hackathon - Sea Ice Team, Contributors: Alek Petty, Andrew Barrett, Xin Miao, Phil McDowall, Vivek*
6 *Balasubramanian, <https://github.com/polar-computing/SeaIce> Is there any relationship between the author's package with the*
7 *XSEDE 2016 package? Please cite it if necessary.*

8 We had not seen that package prior to this review. Our work has no basis in the code referenced. We
9 appreciate being informed about another activity and future collaboration between our efforts and this
10 project may be beneficial to the community. Citation does not seem to be warranted since the code
11 referenced does not appear to be published yet.

12 *L9: What is "dm-scale"?*

13 'dm' here stands for decimeter – the SI term for 10^{-1} meters.

14 *The terms used in manuscript are not consistent. L13: . . . melt ponds and submerged ice, so this is definition used in*
15 *(Miao, 2016). This includes two subclasses: melt pond (MP) and coastal submerged ice. So how did author*
16 *calculate MP coverage in L364? How to extract MP from the broad category of "melt ponds and submerged ice"?*
17 *Please make it clear.*

18 The definition we use for melt ponds is stated in section 3.3.2, line 243 to 244, and we are consistent with
19 the usage throughout the manuscript. Our definition is not the same as that used in Miao et al. (2016), as we
20 do not differentiate between melt ponds and coastal submerged ice. We explicitly clarify this difference on
21 lines 245-249. From a shortwave optical albedo standpoint it is unnecessary to separate these classes, and
22 therefore we do not attempt to extract melt ponds according to this narrower definition. Other works
23 present methods to separate these (Miao et al., 2015, for example) that could be applied to the results
24 presented here for users interested in that application.

25 We have changed the category name to be "melt ponds and submerged ice" to alleviate some of the
26 confusion for this category.

27 *L165: Did author consider the possible image distortion due to tilting of sRGB and other images?*

28 For this work, no. As we are not trying to answer any scientific questions based on this sRGB imagery
29 specifically, we did not attempt to correct image distortions. The algorithm is able to classify images even
30 with small amounts of off-nadir distortion. Applications that seek to use sRGB imagery to answer scientific
31 questions should address any image distortion present. As sRGB imagery is not standard (unlike
32 WorldView), correcting image distortion must be done on a case by case basis using positioning, pointing,
33 and lens information which was not available in the data we worked with.

34 *L225: One of the major feature of RF is that it only need a small amount of samples, very suitable in labor-intensive*
35 *remote sensing project like sea ice detection.*

36 This is true: We have added "[...] even with relatively small training datasets" to line 228.

37 *L236: How did you separate regular melt pond (fresh water) and melt-through MP (salt water)? Why not use the*
38 *technique provided in (Miao, 2016)?*

39 We did not differentiate between fresh water melt ponds and salt water melt ponds. Our motivation lies in
40 short wave optical properties of melt ponds and from that perspective the distinction between salt and fresh
41 water is not important. We added line 241 to clarify this: "Our surface type definitions focus on the
42 behavior of a surface in absorption of shortwave radiation and radiative energy transfer". However, melt
43 ponds that are completely melted through were classified as open water based on their unique spectral
44 characteristics (Figure 5).

45 *L 256: I think it makes sense to combine 3.3.4 and 3.3.5 to 3.3.3.*

46 Thank you for the suggestion. We have combine sections 3.3.4 and 3.3.5 into a single section describing all
47 of the attributes calculated for each image object.

48 *L191&L255: Did author consider the shadow issues? Shadow is an interesting sea ice feature, please refer to Xin*
49 *Miao, Hongjie Xie, Stephen F. Ackley, Songfeng Zheng, "Object-Based Arctic Sea Ice Ridge Detection From High-*
50 *Spatial-Resolution Imagery", IEEE Geoscience and Remote Sensing Letters, 13(6): 787-791, 2016.*

51 *L307: Can you provide an example? I don't understand why.*

52 In lines 259-265 we have edited the description of shadow detection to better illustrate our approach, and in
53 lines 316-323 we have edited the description of detecting ridges in neighboring regions.

54 Shadows are an interesting feature of sea ice, but classification of shadow regions is beyond the scope of
55 this paper. We are not trying to present shadow or ridge detection as a stand-alone feature. In spring
56 panchromatic WorldView imagery, shadows look similar to melt ponds, and lines 259-265 is a simple
57 method to address the similarity.

58 The example presented in line 316 (was 307) is an example of how using neighborhood statistics help
59 identify the classification of an object, and we have reworded it this to be more apparent.

60 *L367: Section 3.6 is very confusing. What do you mean by "larger sample"? Is it "larger number of samples"?*
61 *What is "metric" here? L374: you mean 'observer' not 'user', rite?*

62 We agree that this section as written was confusing, and we have restructured much of this paragraph to
63 increase its clarity. The larger sample assessed the accuracy of 1000 pixels instead of 100. User and
64 observer were referring to the same thing, and we have simplified this to a single term.

65 *L381: Figure 7 refer to Figure 8? Very confusing here.*

66 No, but there was a typo in describing Figure 7 here. This sentence has been edited to be more precise in its
67 reference to Figure 7.

68 *L 389: Fig. 8??*

69 This line correctly references Figure 8. We have rearranged the order of this sentence to be more clear.

70 *L405: Only 4.1 not 4.2? Then author could remove this subtitle.*

71 We've added a section 4.1 here to divide this section into 4.1 and 4.2

72 *Comment: L596: Very positive contribution by sharing the training set!*

73 Thank you!

Open Source Algorithm for Detecting Sea Ice Surface Features in High Resolution Optical Imagery

Nicholas C. Wright¹, Christopher M. Polashenski^{1,2}

¹Thayer School of Engineering, Dartmouth College, Hanover, NH, USA

²U.S. Army Cold Regions Research and Engineering Laboratories, Hanover, NH, USA

Correspondence to: N. C. Wright (ncwright.th@dartmouth.edu)

Abstract. Snow, ice, and melt ponds cover the surface of the Arctic Ocean in fractions that change throughout the seasons. These surfaces control albedo and exert tremendous influence over the energy balance in the Arctic. Increasingly available m- to dm-scale resolution optical imagery captures the evolution of the ice and ocean surface state visually, but methods for quantifying coverage of key surface types from raw imagery are not yet well established. Here we present an open source system designed to provide a standardized, automated, and reproducible technique for processing optical imagery of sea ice. The method classifies surface coverage into three main categories: Snow and bare ice, melt ponds and submerged ice, and open water. The method is demonstrated on imagery from four sensor platforms and on imagery spanning from spring thaw to fall freeze-up. Tests show the classification accuracy of this method typically exceeds 96%. To facilitate scientific use, we evaluate the minimum observation area required for reporting a representative sample of surface coverage. We provide an open source distribution of this algorithm and associated training data sets and suggest the community consider this a step towards standardizing optical sea ice imagery processing. We hope to encourage future collaborative efforts to improve the code base and to analyze large datasets of optical sea ice imagery.

1 Introduction

The surface of the sea ice-ocean system exhibits many different forms. Snow, ice, ocean, and melt ponds cover the surface in fractions that change throughout the seasons. The relative fractions of these surfaces covering the Arctic ocean are undergoing substantial change due to rapid loss of sea ice (Stroeve et al., 2012), increase in the duration of melt (Markus et al., 2009; Stroeve et al., 2014), decrease in sea ice age (Maslanik et al., 2011), and decrease in sea ice thickness (Kwok and Rothrock, 2009; Laxon et al., 2013) over recent decades. As a whole, the changes are reducing albedo and enhancing the absorption of solar radiation, triggering an ice albedo feedback (Curry et al., 1995; Perovich et al., 2008; Pistone et al., 2014). Large-scale remote sensing has been instrumental in documenting the ongoing change in ice extent (Parkinson and Comiso, 2013), thickness (Kurtz et al., 2013; Kwok and Rothrock, 2009; Laxon et al., 2013), and surface melt state (Markus et al., 2009). An increasing focus on improving prediction of future sea ice and climate states, however, has also created substantial interest in better observing, characterizing, and modeling the *processes* that drive changes in albedo-relevant sea ice surface conditions such as melt pond formation, which occur at smaller length scales. For these, observations that resolve surface conditions explicitly are needed to understand the underlying causes of the seasonal and spatial evolution of albedo in a more sophisticated way.

34 Explicitly sensing the key aspects of the sea ice surface, including melt pond coverage, degree of deformation, floe
35 size, and lead distributions, requires evaluating the surface at meter to decimeter scale resolution. Variability in the
36 spatial coverage and morphology of these surface characteristics, however, occurs over hundreds of meters to tens of
37 kilometers. Estimates of aggregate scale surface coverage fraction must therefore be made at high resolution over
38 sample domains of many square kilometers. Quantifying the relative abundance of surface types over domains of
39 multi-kilometer scale from manned ground campaigns is both time consuming and impractical. Remote sensing
40 provides a more viable approach for studying these multi-kilometer areas. High resolution optical imagery (e.g. Figure
41 1) visually captures the surface features of interest, but the methods for analyzing this imagery remain under-
42 developed.

43 The need for remote sensing methods enabling quantification of meter-scale sea ice surface characteristics has
44 been well recognized, and efforts have been made to address it. Recent developments in remote sensing of sea ice
45 surface conditions fall into two categories: (1) methods using low-medium resolution satellite imagery (i.e. having
46 pixel sizes larger than the typical ice surface feature size) with spectral un-mixing type algorithms to derive aggregate
47 measures of sub-pixel phenomena (e.g. for melt ponds Markus et al., 2003; Rösel et al., 2012; Rösel and Kaleschke,
48 2011; Tschudi et al., 2008) and (2) methods using higher resolution satellite or airborne imagery (i.e. having pixel size
49 smaller than the typical scale of ice surface features) that is capable of explicitly resolving features (e.g. [Arntsen et
50 al., 2015](#); [Fetterer and Untersteiner, 1998](#); [Inoue et al., 2008](#); [Kwok, 2014](#); [Lu et al., 2010](#); [Miao et al., 2015](#); [Perovich
51 et al., 2002b](#); [Renner et al., 2014](#); [Webster et al., 2015](#)). The first category, those derived from low-medium resolution
52 imagery, have notable strengths in their frequent sampling and basin-wide coverage. They cannot, however, provide
53 detailed statistics on the morphology of surface [features](#) necessary for assessing our process-based understanding and
54 have substantial uncertainty due to ambiguity in spectral signal un-mixing. The second category – observations at high
55 resolutions which explicitly resolve surface properties – can provide these detailed statistics, but were historically
56 limited by a dearth of data acquisitions. Recent increases in imagery availability from formerly classified defense
57 (Kwok, 2014) or commercial satellites (e.g. DigitalGlobe), and increases in manned flights over the Arctic (e.g.
58 IceBridge, SIZRS) have substantially reduced this constraint for optical imagery. Likely increases in collection of
59 imagery from UAV's (DeMott and Hill, 2016) and increases in satellite imaging bandwidth (e.g. DigitalGlobe
60 WorldView 4 launched in 2016) suggest that availability of high resolution imagery will continue to increase.

61 Processing high resolution sea ice imagery to derive useful metrics quantifying surface state, however, remains a
62 major hurdle. Recent years have seen numerous publications demonstrating the success of various processing
63 techniques for optical imagery of sea ice on limited test cases (e.g. Inoue et al., 2008; Kwok, 2014; Lu et al., 2010;
64 Miao et al., 2015; Perovich et al., 2002b; Renner et al., 2014; Webster et al., 2015). None of these techniques, however,
65 have been adopted as a standard or been used to produce large-scale datasets, and validation has been limited.
66 Furthermore, none have been challenged by imagery collected across the seasonal evolution of the ice or used to
67 process data from multiple sensor platforms. These issues must be addressed to enable in large scale production-type
68 image processing and use of high resolution imagery as a sea ice monitoring tool.

69 A unique aspect of high resolution sea ice imagery datasets, which differs from most satellite remote sensing, is
70 the quantity of image sources and data owners. Distributed collection and data ownership means centralized processing

Deleted: Inoue et al., 2008; Kwok, 2014; Lu et al., 2010; Miao et al., 2015; Perovich et al., 2002; Renner et al., 2014; Webster et al., 2015)

Deleted: conditions

75 of imagery to produce a single product is unlikely. Instead, we believe that distributed processing by dataset owners
76 is more likely and the community therefore has a substantial need for a shared, standard processing protocol.
77 Successful creation of such a processing protocol would increase imagery analysis and result in the production of
78 datasets suitable for ingestion by models to validate surface process parameterizations. In this paper, we assess
79 previous publications detailing image processing methods for remote sensing and present a novel scheme that builds
80 from the strengths and lessons of prior efforts. Our resulting algorithm, the Open Source Sea-ice Processing (OSSP)
81 Algorithm, is presented as a step toward addressing the community need for a standardized methodology, and released
82 in an open source implementation for use and improvement by the community.

83 We began with three primary design goals that guided our development of the image processing scheme. The
84 method must (1) have a fully automatic workflow and have a low barrier to entry for new users, (2) produce accurate,
85 consistent results in a standardized output format, and (3) be able to produce equivalent geophysical parameters from
86 a range of disparate image acquisition methods. To meet these goals, we have packaged OSSP in a user-friendly
87 format, with clear documentation for start-up. We include a set of default parameters that should meet most user needs,
88 permitting processing of pre-defined image types with minimal set-up. The algorithm parameters are tunable to allow
89 more advanced users to tailor the method to their specific imagery input. We chose an open source format to enhance
90 the ability for the community to explore and improve the code relative to a commercial software. Herein, we discuss
91 how we arrived at the particular technique we use, and why it is superior to some other possible mechanisms. We then
92 demonstrate the ability of this algorithm to analyze imagery of disparate sources by showing results from high
93 resolution DigitalGlobe WorldView satellite imagery in both panchromatic and pansharpened formats, aerial sRGB
94 (standard Red, Green, Blue) imagery, and NASA Operation IceBridge DMS (Digital Mapping System) optical
95 imagery. In this paper, we classify imaged areas into three surface types: Snow and ice, melt ponds and submerged
96 ice, and open water. The algorithm is, however, suitable for classifying any number of categories, should a user be
97 interested in different surface types, and might be adapted for use on imagery of other surface types.

98 **2 Algorithm Design**

99 Two core decisions were faced in the design of this image classification scheme: (1) Whether to analyze the image by
100 individual pixels or to analyze objects constructed of similar, neighboring pixels, and (2) which algorithm to use for
101 the classification of these image units.

102 Prior work [in terrestrial remote sensing applications](#) has shown that object-based classifications are more accurate
103 than single pixel classifications when analyzing high-resolution imagery (Blaschke, 2010; Blaschke et al., 2014; Duro
104 et al., 2012; Yan et al., 2006). In this case, 'high resolution' has a specific definition dependent on the relationship
105 between the size of pixels and objects of interest. An image is high resolution when surface features of interest are
106 substantially larger than pixel resolution and therefore are composed of many pixels. In such imagery, objects, or
107 groups of pixels constructed to contain only similar pixels (i.e. a single surface type), can be analyzed as a set. The m-
108 dm resolution imagery meets this definition for features like melt ponds and ice floes. Object based classification
109 enables an algorithm to extract information about image texture and spatial correlation within the pixel group;

110 information that is not available in single pixel based classifications and can enhance accuracy of surface type
111 discrimination. Furthermore, object based classifications are much better at preserving the size and shape of surface
112 cover regions. Classification errors of individual pixel schemes tend to produce a ‘speckled’ appearance in the image
113 classification with incorrect pixels scattered across the image. Errors in object based classifications, meanwhile,
114 appear as entire objects that are mislabeled (Duro et al., 2012). Since our intent is to process high-resolution imagery
115 and produce measurements not only of the areal fractions of surface type regions, but also to enable analysis of the
116 size and shape of ice surface type regions (e.g. for floe size or melt pond size determination), the choice of object
117 based classification over pixel based was clear.

118 A wide range of algorithms were considered for classifying image objects. We first considered the use of
119 supervised versus an unsupervised classification schemes. Unsupervised schemes were rejected as they produce
120 inconsistent, non-intercomparable results. These schemes, such as clustering algorithms, group observations into a
121 predefined number of categories – even if not all feature types of interest are present in an image. For example, an
122 image containing only snow-covered ice will still be categorized into the same number of classes as an image with
123 snow, melt ponds, and open water together – resulting in multiple classes of snow. Since the boundary between classes
124 also changes in each image, standardizing results across imagery with different sources and of scenes with different
125 feature content would be challenging at best.

126 Supervised classification schemes instead utilize a set of known examples (called training data) to assign a
127 classification to unknown objects based on similarity to user-identified objects. Supervised classification schemes
128 have several advantages. They can produce fixed surface type definitions, allow for more control and fine tuning of
129 the algorithm, improve in skill as more points are added to the training data, and allow users to choose what surface
130 characteristics they wish to classify. While many machine learning techniques have shown high accuracy in remote
131 sensing applications (Duro et al., 2012), we selected a random forest machine learning classifier over other supervised
132 learning algorithms for its ability to handle nonlinear and categorical training inputs (Breiman, 2001; DeFries, 2000;
133 Pal, 2005), resistance to outliers in the training dataset (Breiman, 1996), and relative ease of implementation.

134 Our scheme, learning from the success of Miao et al. (2015) in classifying aerial imagery, uses an image
135 segmentation algorithm to divide the image into objects which are then classified with random forest machine learning.
136 Our implementation of the segmentation and classification, however, were custom-built using well known image
137 processing tools (Pedregosa et al., 2011; van der Walt et al., 2014) in an open source format. We do not attempt to
138 assert that our method is the optimal method for processing sea ice imagery. Instead, we argue that it is easily usable
139 by the community at large, produces highly accurate and consistent results, and merits consideration as a standardized
140 methodology. In coordination with this publication, we release our code (available at <https://github.com/wrightni/ossip>
141 [doi:10.5281/zenodo.1133689](https://doi.org/10.5281/zenodo.1133689)) with the intention of encouraging movement toward a standardized method. Our hope
142 is to continue development of the algorithm with contributions and suggestions from the sea ice community.

Deleted: examples of which include K-means
Deleted: and maximum likelihood classifiers

Deleted: building on

Deleted: We do not attempt to assert that our method is the optimal method for processing sea ice imagery. Instead, we argue that it is easily usable by the community at large, produces highly accurate and consistent results, and merits consideration as a standardized methodology.

151 **3 Methods**

152 **3.1 Image Collection and Preprocessing**

153 The imagery used to test the algorithm was selected from four distinct sources in order to assess the algorithm’s ability
154 to deliver consistent and intercomparable measures of geophysical parameters. We chose high resolution satellite
155 imagery from DigitalGlobe’s WorldView constellation in panchromatic and 8 band multispectral formats, NASA
156 Operation IceBridge Digital Mapping System optical imagery, and aerial sRGB imagery collected using an aircraft-
157 mounted standard DSLR camera as part of the SIZONet project. We first demonstrate the technique’s ability to handle
158 imagery representing all stages of the seasonal evolution of sea ice conditions on a series of 22 panchromatic satellite
159 images collected between March and August of 2014 at a single site in the Beaufort Sea: 72.0° N 128.0° W. We then
160 process 4 multispectral WorldView 2 images of the same site, each collected coincident with a panchromatic image
161 and compare results to assess the benefit of spectral information. Finally, we process a set of 20 sRGB images and 20
162 IceBridge DMS images containing a variety of sea ice surface types to illustrate the accuracy of the method on [aerial](#)
163 [image sources](#). [The imagery sources chosen for this analysis were selected to be representative of the variation that](#)
164 [exists in optical imagery of sea ice, but there is an abundance of image data that can be processed with this technique.](#)

Deleted: other image sources.

165 The satellite images were collected by tasking WorldView 1 and WorldView 2 Digital Globe satellites over fixed
166 locations in the Arctic. Tasking requests were submitted to DigitalGlobe with the support and collaboration of the
167 Polar Geospatial Center. The panchromatic bands of WorldView 1 and 2 both have a spatial resolution of 0.46m at
168 nadir. The WorldView 1 satellite panchromatic band samples the visible spectrum between 400 nm and 900 nm, while
169 the WorldView 2 satellite panchromatic band samples between 450 nm and 850 nm. In addition, WorldView 2 has 8
170 multispectral bands at 1.84 m nadir resolution, capturing bands within the range of 400nm to 1040nm. Each
171 WorldView image captures an area of ~700-1300 km². Of the 22 useable panchromatic collections at the site, 15 were
172 completely cloud free while 7 of the images were partially cloudy. Images with partial cloud cover were manually
173 masked and cloud covered areas were excluded from analysis. The aerial sRGB imagery was captured along a 100km
174 long transect to the north of Barrow, Alaska with a Nikon D70 DSLR mounted at nadir to a light airplane during June
175 2009. The IceBridge imagery was collected in July of 2016 near 73° N 171° W with a Canon EOS 5D Mark II digital
176 camera. We utilize the L0 (raw) DMS IceBridge imagery, which has a 10cm spatial resolution when taken from 1500
177 feet altitude (Dominguez, 2010, updated 2017).

178 Each satellite image was orthorectified to mean sea level before further processing. Orthorectification corrects for
179 image distortions caused by off-nadir acquisition angles and produces a planimetrically correct image that can be
180 accurately measured for distance and area. Due to the relatively low surface roughness of both multiyear and first year
181 sea ice (Petty et al., 2016), errors induced by ignoring the real topography during orthorectification are small.
182 Multispectral imagery was pansharpened to the resolution of the panchromatic imagery. Pansharpening is a method
183 that creates a high resolution multispectral image by combining intensity values from a higher resolution panchromatic
184 image with color information from a lower resolution multispectral image. The pansharpened imagery used here was
185 created using a ‘weighted’ Brovey algorithm. This algorithm resamples the multispectral image to the resolution of
186 the panchromatic image, then each pixel’s [value](#) is multiplied by the ratio of the corresponding panchromatic pixel

Deleted: value

189 value to the sum of all multispectral pixel values. The orthorectification and pansharpener scripts were developed by
190 the Polar Geospatial Center at the University of Minnesota and utilize the GDAL (Geospatial Data Abstraction
191 Library) image processing tools (GDAL, 2016). All imagery used was rescaled to the full 8-bit color space for
192 improved contrast and viewing. No other preprocessing was done to the aerial sRGB imagery or IceBridge DMS
193 imagery.

194 3.2 Image Segmentation

195 A flow chart of the image processing steps taken after pre-processing is presented in Fig. 2. The first task in the image
196 processing algorithm is to segment the image into groups of similar pixels, called objects. Accurate segmentation
197 requires finding the boundaries between the natural surface types we wish to differentiate (e.g. the boundary between
198 ice covered and open ocean), delineating their locations, and using these boundaries to produce image objects. Sea ice
199 surface types have large differences in reflectivity and tend to change abruptly, rather than gradually over a large
200 distance. We exploit this characteristic by using an edge detection algorithm to find boundaries between surface types.
201 Figure 3 contains a visual demonstration of this process. First, a Sobel-Feldman operator (van der Walt et al., 2014)
202 is applied to the input image (Fig. 3a). The Sobel-Feldman filter applies a discrete differentiation kernel across the
203 image to find the local gradient of the image intensity. High gradient values correspond to abrupt changes in pixel
204 intensity, which are likely boundaries between surface types. We scale the gradient values by an amplification factor
205 of 2 in order to further highlight edge regions in the image. Following the amplification, we threshold the lowest 10%
206 of the gradient image and set the values to zero. This reduces noise detected by the Sobel-Feldman filter, and eliminates
207 weaker edges. The amplification factor and gradient threshold percentage are both tuning parameters, which can be
208 adjusted to properly segment images based on the input image and the strength of edges sought.

209 The strongest edges in optical imagery of sea ice are typically the ocean-ice interface, followed by melt pond-ice
210 boundaries, then ice ridges and uneven ice surfaces. In general, the more edges detected, the more segmented the
211 image will become, and the more computational resources required to later classify the [increased number of](#) image
212 objects. On the other hand, an under-segmented image may miss the natural boundaries between surfaces. Under
213 segmentation introduces classification error because an object containing two surface types cannot be correctly
214 classified. An optimally segmented image is one which captures all the natural surface boundaries with minimal over-
215 segmentation (i.e. boundaries placed in the middle of features). The appropriate parameters for our imagery were
216 tuned by visual inspection of the segmentation results. In such inspection, desired segmentation lines are manually
217 drawn, and algorithm-determined segmentation lines are overlain and evaluated for completeness.

218 The result of the edge detection is a gradient map that marks the strength of edges in the image. We use a watershed
219 segmentation technique to build complete objects based on edge locations and intensity (van der Walt et al., 2014).
220 We first calculate all local minimum values in the gradient image, where a marker is then placed to indicate the origin
221 of watershed regions. Each region then begins iteratively expanding in all directions of increasing image gradient until
222 encountering a local maximum in the gradient image or encountering a separately growing region. This continues until
223 every pixel in the image belongs to a unique set. With the proper parameter selection, each object will represent a
224 single surface type. It is often the case that some areas will be over-segmented (i.e. a single surface feature represented

225 by multiple objects). Over segmentation can either be ignored, or objects can be recombined if they meet similarity
226 criteria in an effort to save computational resources. Here we chose to classify objects without recombination. Figure
227 3b shows the detected edges overlain on top of the input image.

228 The watershed segmentation algorithm benefits from the ability to create objects of variable size. Large objects
229 are built in areas of low surface variability while many small objects are created in areas of high variability. This
230 variable object sizing is well suited to sea ice surface classification because the variability of each surface type occurs
231 at different scales. Areas of open water and snow covered first year ice, for example, can often be found in large
232 expanses, while areas that contain melt ponds, ice ridges, or rubble fields frequently cover small areas and are tightly
233 intermingled with other surface types. Variable object sizes give the fine detail needed to capture surfaces of high
234 heterogeneity in their full detail, while limiting over segmentation of uniform areas.

235 3.3 Segment Classification

236 3.3.1 Overview

237 Once the image has been divided into regions of the same surface type, each object must be classified as to which
238 surface type it represents. We classify the objects using a random forest machine learning technique (Breiman, 2001;
239 Pedregosa et al., 2011). The development of a machine learning algorithm requires multiple iterative steps: 1) Select
240 attributes with which to classify each object, 2) create a training dataset, 3) classify unknown image objects based on
241 the training set, and 4) assess performance and refine, starting from step 1. Random forest classifiers excel for their
242 relative ease of use, flexibility in the choice of attributes that define each object, and overall high accuracy, even with
243 relatively small training datasets. The random forest classifier is only one of many available machine learning
244 approaches and others may also be suitable.

Deleted: .

245 3.3.2 Surface Type Definitions

246 Another key challenge to quantitatively monitoring sea ice surface characteristics from high resolution imagery is a
247 lack of standardized surface type definitions. We noted above that high-resolution sea ice imagery comes from many
248 sources; each with different characteristics. As we will see below, each image source will need to have its own training
249 set created by expert human classifiers. The human classifier must train the algorithm according to definitions of each
250 surface type that are broadly agreed upon in the community for the algorithm to be successful in producing
251 intercomparable datasets. While at first the definitions of open water, ice and melt ponds might seem intuitive, many
252 experts in the cryosphere community have differing opinions, especially on transitional states. Deciding where to
253 delineate transitional states is important to standardization. We have established the following definitions for the three
254 surface types we sought to separate, binning transitional states in a manner most consistent with their impact on albedo.
255 Our surface type definitions focus on the behavior of a surface in absorption of shortwave radiation and radiative
256 energy transfer. (1) Open Water (OW): Applied to surface areas that had zero ice cover as well as those covered by
257 an unconsolidated frazil or grease ice. (2) Melt Ponds and Submerged Ice (MPS): Applied to surfaces where a liquid
258 water layer completely submerges the ice. (3) Ice and Snow. Applied to all surfaces covered by snow or bare ice, as
259 well as decaying ice and snow that is saturated, but not submerged. The definition of melt ponds includes the classical

Deleted: challenge these notions

Deleted: (MP

Deleted: (I+S):

264 definition of melt ponds where meltwater is trapped in isolated patches atop ice, as well as optically-similar ice
265 submerged near the edge of a floe. [While previous work separates these categories \(e.g. \(Miao et al., 2015\) we did not](#)
266 [attempt to break these 'pond' types because the distinction is unimportant from a shortwave energy balance \(albedo\)](#)
267 [perspective](#). We further refined the ice and snow category into two sub categories: (3a) Thick Ice and Snow, applied
268 during the freezing season to ice appearing to the expert classifier to be thicker than 50cm or having an optically thick
269 snow cover and to ice during the melt season covered by a drained surface scattering layer (Perovich, 2005) of
270 decaying ice crystals and (3b) Dark and Thin Ice, applied during the freezing season to surfaces of thin ice that are not
271 snow covered including nilas and young ice. This label was also applied during melting conditions to ice covered by
272 saturated slush, but not completely submerged in water. This is ice which in some prior publications (e.g. Polashenski
273 et al., 2012) was labeled as 'slushy bare ice'. We acknowledge that the boundary between the ice and snow sub-
274 categories is often more a continuum than a defined border but note that distinguishing the two types is useful for
275 algorithm accuracy. Dividing the [ice/snow](#) type creates two relatively homogeneous categories rather than a single
276 larger category with large internal differences. A user only interested in the categories of ice, ponds, and open water
277 could simply re-combine them, as we have done for analysis. [We created a temporary 'shadow' classification category](#)
278 that was used [only](#) in panchromatic WorldView images [captured](#) prior to melt onset. This [category](#) allowed the
279 [machine learning](#) algorithm to differentiate dark shadows in spring imagery from melt ponds in summer imagery –
280 surface types that look similar [in single-band imagery](#). [This category is used exclusively as a temporary step in](#)
281 [processing that allows us to bypass masking shadow regions directly \(e.g. \(Webster et al., 2015\). As this is not](#)
282 [designed to be a standalone classification category \(as opposed to Miao et al., 2015, 2016\), objects classified as a](#)
283 [shadow were grouped back with the ice/snow category](#).

Deleted: We did not attempt to break these 'pond' types because the distinction is unimportant from a shortwave energy balance (albedo) perspective.

Deleted:

Deleted: I+S

Deleted: Furthermore, we

Deleted: classification

Deleted: based on single-band pixel intensity values. The shadow category was grouped back with the I+S category for analysis.

284 3.3.3 Attribute Selection

285 Attributes are quantifiable measures of image object properties used by the classifier in discriminating surface types.
286 An enormous array of possible attributes could be calculated for each image object and could be calculated in many
287 ways. Examples of properties that could be quantified as attributes include values of the enclosed pixels, the size and
288 shape of the object, and values of adjacent pixels. The calculation of pixel values aggregated by image objects takes
289 advantage of the additional information held in the pixel group (as compared to individual pixels). We have compiled
290 a list representing a relevant subset of such attributes that can be used to distinguish different surface types in Table
291 1. We included a selection of attributes similar to those used in previous publications (e.g. Miao et al., 2015), as well
292 as attributes we have developed specifically for our algorithm.

293 Each image source provides unique information about the surface and it can be expected that a different list of
294 attributes will be optimal for classification of each image type – even though we seek the same geophysical parameters.
295 [As high-resolution satellite images can have millions of image objects, calculating the](#) attributes of each object [quickly](#)
296 [becomes](#) computationally expensive. We have, therefore, determined those that are most valuable for classifying each
297 image type to use in our classification. For example, pansharpened WorldView 2 imagery has 8 spectral bands which
298 can inform the classification, while panchromatic versions of the same image have only a single band. Our goal was
299 to select a combination of attributes that describe the intensity and textural characteristics of the object itself, and of

Deleted: Calculating

Deleted: image

Deleted: is

312 the area surrounding the object. Table 1 indicates which attributes were selected for use in classifying each image
313 type.

314 We selected attributes by only including those with a high relative importance. The importance of each attribute
315 is a property of a random forest classifier, and is defined as the number of times a given attribute contributed to the
316 final prediction of an input. After initial tests with large numbers of attributes, we narrowed our selection by using
317 only those attributes that contributed to a classification in greater than 1% of cases. For discussion here, we group the
318 attributes into two broad categories: Those calculated using internal pixels alone (object attributes), and those
319 calculated from external pixel values (neighbor attributes).

320 3.3.4 Object Attributes

321 The most important attributes in the classification of an image segment were found to be aggregate measures of pixel
322 intensity within the object. We determine these by analyzing the mean pixel intensity of all bands and the median of
323 the panchromatic band. An important benefit of image segmentation is the ability to calculate estimates of surface
324 texture by looking at the variability within a group of pixels. The texture is often unique in the different surface types
325 we seek to distinguish. Open water is typically uniformly absorptive and has minimal intensity variance. Melt ponds,
326 in contrast, come in many realizations and exhibit a wider range in reflectance, even within individual ponds. To
327 estimate surface texture, we calculate the standard deviation of pixel intensity values and the image entropy within
328 each segment. Image entropy, H , is calculated as

329
$$H = - \sum p * \log_2 p$$

330 where p represents the bin counts of a pixel intensity histogram within the segment. We also calculate the size of each
331 segment as the number of pixels it contains. As sea ice surface characteristics evolve appreciably over time,
332 particularly before and after melt onset, we use image acquisition date as an attribute in for classification. While date
333 of melt onset varies, and the reader might argue that a more applicable attribute would be image melt state, melt state,
334 is not an apriori characteristic of the image. It would therefore need to be manually defined, and not meet our demand
335 for a fully automated scheme.

336 In multispectral imagery, we also calculate the ratios between the mean absorption of each object in certain
337 portions of the spectrum. The important band ratios used for the multispectral WorldView imagery were determined
338 empirically. We tested every possible band combination, and successively removed the ratios that did not contribute
339 to more than 1% of object classifications. In sRGB imagery we use the band ratios shown to be informative in this
340 application by Miao et al. (2015).

341 In addition to information contained within each object, we utilize information from the surrounding area. To
342 analyze the surrounding region, we determine the dimensions of a minimum bounding box that contains the object,
343 then expand the box by five pixels in each direction. All pixels contained within this box, minus those in the object,
344 are considered to be neighboring pixels. Analogous to the internal attribute calculations, we find the average intensity
345 and standard deviation of these pixels. We also calculate the maximum single intensity within the neighboring region.
346 Searching for attributes outside of the object improves the algorithm's predictive capabilities by providing spatial
347 context. Bright neighboring pixels (as an analog for an illuminated ridge) often provide information to distinguish, for

Deleted: We include image date as an attribute because

Deleted: pond formation

Deleted: . Since

Deleted: . Melt

Deleted: however,

Deleted: and

Deleted: therefore

Deleted: meeting

Deleted: segment

Deleted: segment

Deleted: 3.3.5 Neighbor Attributes .

Deleted: segment

Deleted: segment

Deleted: segment

Deleted: this

Deleted: , which measures

Deleted: the presence

Deleted: neighboring

Deleted: . The maximum neighboring intensity

Deleted: provides

368 example, a shadowed ice surface from a melt pond. In panchromatic imagery, [melt ponds and shadows appear similar](#)
369 when evaluated solely on internal [object](#) attributes. [However, a dark region with an immediately adjacent bright region](#)
370 [is more likely to be a shadow than a dark region not adjacent to a bright pixel \(e.g. a pond\)](#). We do note that it is likely
371 that a more complex algorithm, for example identifying those pixels in a radius or distance to the edge of the segment,
372 rather than using a bounding box, would be more reliable. The tradeoff, however, is one of higher computational
373 expense.

Deleted: these regions are often

Deleted: segment

374 3.4 Training Set Creation

375 Four training datasets were created to analyze the images selected for this paper. One training set was created for
376 each imagery source: Panchromatic satellite imagery, multispectral satellite imagery, aerial sRGB imagery, and
377 IceBridge DMS imagery. Each training set consists of a list of image objects that have been manually classified by a
378 human and a list of attribute values calculated from those objects and their surroundings. The manual classification is
379 carried out by multiple sea ice experts. Experienced observers of sea ice can classify the majority (85%+) of segments
380 in a high resolution optical image with confidence. To address the ambiguity in correct identification of certain
381 segments, however, we used several (4) skilled sea ice observers to repeatedly classify image objects. For the initial
382 creation of our training datasets, two of the users had extensive training in the OSSP algorithm and surface type
383 definitions, while the other two [no experience with the algorithm](#). [Users in both categories were briefed on the standard](#)
384 [surface type definitions used for this study \(section 3.3.2\)](#). Figure 4 shows a confusion matrix to compare user
385 classifications. Cells in the diagonal indicate agreement between users, while off- diagonal cells indicate disagreement
386 [\(Pedregosa et al., 2011\)](#). Agreement between the two well-trained users was high (average 94% of segment
387 identifications; Fig. 4a), while the agreement between a well-trained user and a new user was lower (average of 86%;
388 [Fig 4b](#)). After an in-person review of the training objects among all four users, the overall agreement rose to 97%. The
389 remaining 3% of objects were cases where the expert users could not agree on a single classification, even after review
390 of the surface type definitions and discussion. These objects were therefore not used in the final training set. Figure 5
391 shows a series of surface types that span all our classification categories, including those where the classification is
392 clear and those where it is difficult. Difficult segments are over-represented in these images for illustrative purposes,
393 and represent a relatively small fraction of the total surface.

Deleted: had only a brief (i.e. <10 minute) introduction to the surface type definitions and

Deleted: (Pedregosa et al., 2011)

Deleted: ig

394 While the skill of the machine learning prediction increases substantially as the size of the training set grows,
395 creating large training sets is time consuming. We found that training datasets of approximately 1000 points yielded
396 accurate and consistent results. We have developed a graphical user interface (GUI) to facilitate the rapid creation of
397 large training sets (see Fig. 6). The GUI presents a user with the original image side by side with an overlay of a single
398 segment on that image. The user assigns a classification to the segment by visual determination.

399 The training dataset is a critical component of our algorithm because it directly controls the accuracy of the
400 machine learning algorithm – and using a consistent training set is necessary for producing intercomparable results.
401 In coordination with this publication we are releasing our version 1.0 training datasets with the intention that they
402 would represent a first version of *the* standard training set to use with each image type. Though we have found this

409 training dataset robust through our error analyses below, it is our intention to solicit broader input from the community
410 to refine and expand the training datasets available and release future improved versions.

411 In addition to cross-validating the creation of a training dataset between users, we assess the quality of our training
412 set through an out-of-bag (OOB) estimate, which is an internal measure of the training set's predictive power. The
413 random forest method creates an ensemble (forest) of classification trees from the input training set. Each classification
414 tree in this forest is built using a random bootstrap sample of the data in the training set. Because training samples are
415 selected at random, each tree is built with an incomplete set of the original data. For every sample in the original
416 training set, there then exists a subset of classifiers that do not contain that sample. The error rate of each classifier
417 when used to predict the samples that were left out is called the OOB estimate (Breiman, 2001). The OOB estimate
418 has been shown to be equivalent to predicting a separate set of features and comparing the output to a known
419 classification (Breiman, 1996).

420 3.5 Assigning Classifications

421 Once the training dataset is complete, the algorithm is prepared to predict the classification of unknown objects in the
422 images. The random forest classifier is run and a classified image is created by replacing the values within each
423 segment by the classification label predicted. Figure 3c shows the result of labeling image objects with their predicted
424 classification. From the classified image, it is possible to produce a number of useful statistics. The most basic
425 measurement is the total pixel counts for each of the three surface categories. This provides both the total area, in
426 square kilometers, that each surface covers, and the fraction of each image that is covered by each surface type. It
427 would also be possible to calculate measurements such as the average segment size for each surface, melt pond size
428 and connectivity, or floe size distributions. Each of these, however, has its own standardization problems significant
429 enough to merit their own paper.

430 For demonstration, we have used the output from our image classification to calculate the fractional melt pond
431 coverage for each date. The melt pond fraction was defined as the area of melt ponds [and submerged ice](#) divided by
432 the total area covered by ice floes, i.e.:

433
$$\text{Melt Pond Coverage} = \frac{\text{Area}_{MPS}}{\text{Area}_{MPS} + \text{Area}_{I+S}}$$

434 where the subscript [MPS](#) indicates predicted melt ponds [and submerged ice](#) and I+S indicates predicted ice and snow.

435 3.6 Determining Classification Accuracy

436 The primary measure of classification accuracy was to test the processed imagery on a per pixel basis against human
437 classification. For [every](#) processed image, we selected a simple random sample of 100 pixels [chosen](#) from the [whole](#)
438 image and asked four sea ice experts to assign a classification to those pixels. [For a single image from](#) each image
439 source, we also [asked the sea ice experts to classify and additional 900](#) pixels. [This](#) larger sample was created to
440 demonstrate a tighter confidence interval, while the smaller samples were chosen to demonstrate consistency across
441 images. [We used the same GUI developed to create training datasets to assess pixel accuracy.](#) [Pixels](#) were presented
442 [at random](#) to the user by showing the original image with the given pixel highlighted. The [user](#) then identified which

- Deleted: $Area_{MP}$
- Deleted: MP
- Deleted: MP
- Deleted: each
- Deleted: entire
- Deleted: Note that in this case experts are asked to classify individual pixels, rather than segments as they were asked to do in training set creation. For
- Deleted: ,
- Deleted: selected one scene from which to check
- Deleted: classification of a larger sample of 1000
- Deleted: The
- Deleted: in the accuracy
- Deleted: This metric gives a spatially weighted accuracy by assessing individual pixels regardless of how the image was segmented. The pixels
- Deleted: observer

460 of the surface type categories best described that pixel. This assignment is then compared to the algorithm's prediction
461 behind the scenes. The accuracy, as determined by each of the four experts, was averaged to create a composite
462 accuracy for each image.

- Deleted: three
- Deleted: without feedback to
- Deleted: human classifier.
- Deleted: observers

463 4 Results

- Deleted:

464 4.1 Classification of Four Imagery Sources

465 The OSSP image processing method proved highly suitable for the task of classifying sea ice imagery. A visual
466 comparison between the raw and processed imagery, shown in Fig. 7 can quickly demonstrate this in a qualitative
467 sense. Figure 7 contains a comparison between the original and classified imagery for each source, selected to show
468 the performance of the algorithm on images that contain a variety of surface types. The colors shown correspond to
469 the classification category; regions colored black are open water, blue regions are melt ponds and submerged ice, gray
470 regions are wet and thin ice, and white regions are snow and ice. The quantitative processing results, including surface
471 distributions and classification accuracy are shown in Table 2. The overall classification accuracy was $96 \pm 3\%$ across
472 20 IceBridge DMS images; $95 \pm 3\%$ across 20 aerial sRGB images; $97 \pm 2\%$ across 22 panchromatic WorldView 1
473 and 2 images; and $98 \pm 2\%$ across 4 multispectral WorldView 2 images.

- Deleted: two comparisons
- Deleted: imagery

474 The nature of the classification error is presented using a confusion matrix that compares the algorithm
475 classification with a manual classification for 1000 randomly selected pixels. Four confusion matrices, one for a single
476 image from each of the four image sources is shown in Fig. 8. Values along the diagonal of the square are the
477 classifications where the algorithm and the human observer agreed, while values in off-diagonal areas indicate
478 disagreement. Concentration of error into a particular off-diagonal cell helps illustrate the types of confusion the
479 algorithm experiences. The number of pixels that fall into off-diagonal cells is low across all imagery types. In the
480 IceBridge imagery, there is a slight tendency for the algorithm to classify surfaces as open water where a human would
481 choose melt pond. This is caused by exceptionally dark melt ponds on the edge of melting through (Fig. 5, panels F
482 and I). Classification of multispectral WorldView imagery has a small bias towards classifying melt ponds over dark
483 or thin ice (Fig. 5, panel D). Aerial sRGB and Panchromatic WorldView images do not have a distinct pattern to their
484 classification errors.

- Deleted: of
- Deleted: One
- Deleted: matrix is shown in Fig. 8

485 The internal metric of classification training dataset strength, the Out of Bag Error (OOB) estimates, on a 0.0 to
486 1.0 scale, are shown in Table 3 for the trees built from our three training sets. The OOB estimate represents the mean
487 prediction error of the random forest classifier, i.e. an OOB score of 0.92 estimates that the decision tree would predict
488 92% of segments that are contained in the training dataset correctly. The discrepancy between OOB error and the
489 overall classification accuracy is a result of more frequent misclassification of smaller objects; overall accuracy is area
490 weighted, while the OOB score is not.

491 4.2 WorldView: Analyzing A Full Seasonal Progression

- Deleted: 1

492 We analyzed 22 images at a single site in the Beaufort Sea collected between March and August of 2014 to challenge
493 the method with images that span the seasonal evolution of ice surface conditions. The site is Eulerian; it observes a

- Deleted: The

506 [single location in space rather than following a single ice floe through its lifecycle as it drifts](#). Still, the results of these
507 image classifications (shown in Fig. 9) illustrate the progression of the ice surface conditions in terms of our four
508 categories over the course of a single melt season. While cloud cover impacted the temporal continuity of satellite
509 images collected at this site, we are still able to follow the seasonal evolution of surface features. A time series of
510 fractional melt pond coverage calculated from the satellite image site is plotted in Fig. 10. The melt pond coverage
511 jumps to 22% in the earliest June image, as initial ponding begins and floods the surface of the level first year ice.
512 This is followed by a further increase to 45% coverage in the next few days. The melt pond coverage then drops back
513 down to 30% as melt water drains from the surface and forms well defined ponds. The evolution of melt pond coverage
514 over our satellite observation period is consistent with prior field observations (Eicken, 2002; Landy et al., 2014;
515 Polashenski et al., 2012) and matches the four stages of ice melt first described by Eicken (2002). The ice at this
516 observation site fully transitions to open water by mid-July, though it appears that the ice is advected out of the region
517 in the late stages of melt rather than completing melt at this location.

518 5 Discussion

519 5.1 Error

520 There are four primary sources of error in the OSSP method as presented, two internal to the method and two external.
521 Internal error is caused by segment misclassification and by incomplete segmentation (i.e. leaving pixels representing
522 two surface types within one segment). The net internal error was quantified in section 3.6 and 4. External error is
523 introduced by pixilation – or blurring of real surface boundaries due to insufficient image resolution – and human
524 error in assigning a ‘ground truth’ value to an aerial or satellite observation during training.

525 5.1.1 Internal Error

526 Through assessing the accuracy of each classified image on a pixel-by-pixel basis (section 3.6), we collect all internal
527 sources of error into one measurement: The algorithm either [assigned the same classification as a human would have](#),
528 or it did not. Total internal accuracy calculated for the method, relative to human classifiers, is quite good, at 90-99%
529 across all image types. Our experience is that this level of accuracy approaches the accuracy with which fractional
530 surface coverage can practically be determined from labor intensive ground campaign techniques such as lidar and
531 measured linear transects (e.g. Polashenski et al., 2012)

532 [The first type of internal error is misclassification error, where the image classification algorithm fails to assign](#)
533 [the same classification that a human expert would choose](#). This type of error is best quantified by analyzing the training
534 datasets. The OOB score for each forest of decision trees (Table 3) provides an estimate of each forest’s ability to
535 correctly predict objects similar to those used to create the forest (section 3.4). The OOB score is not influenced by
536 segmentation error, because the objects selected for training dataset use were filtered to remove any objects that
537 contained more than one surface type. The most commonly misapplied category was the Dark and Thin Ice
538 subcategory of Ice and Snow. This category often represents surface types that are in a transitional state, and is often
539 difficult to classify even for a human observer.

Deleted: classified each pixel

Deleted: way

Deleted: the

Deleted: Misclassification error, the

Deleted: occurs when

Deleted: replicate the

Deleted: experts’ decision-making process

547 [The second type of internal error is segmentation error, where](#) an object is created that contains more than one of
548 the surface types we are trying to distinguish. This occurs when boundaries between objects are not placed where
549 boundaries between surfaces exist; an issue most common where one surface type gradually transitions to another.
550 When this occurs, some portion of that object will necessarily be misclassified. We have compensated for areas that
551 lack sharp boundaries by biasing the image segmentation towards over-segmentation, but a small number of objects
552 still contain more than one surface type. During training set creation, we asked the human experts to identify objects
553 containing more than one surface type. 3.5% of objects were identified as insufficiently segmented in aerial imagery,
554 and 2% of objects in satellite imagery. This represents the upper limit for the total percentage of insufficiently
555 segmented objects for several reasons. First, segmentation error was most prevalent in transitional surface types (i.e.
556 Dark and Thin Ice), which represents a small portion of the overall image and is composed of relatively small objects.
557 This category is overrepresented in the training objects because objects were chosen to sample each surface type and
558 not weighted by area. In addition, insufficiently segmented objects are generally composed of only two surface types,
559 and end up identified as the surface which represents more of the object's area. Hence the total internal error introduced
560 by segmentation error is appreciably smaller than misclassification error, likely well under 1%.

561 5.1.2 External Error

562 The first form of external error is introduced by image resolution. At lower image resolutions, more pixels of the
563 image span edges, and smaller features are more likely to go undetected. Pixels on the edge of surface types necessarily
564 represent more than one surface type, but can be classified as only one. Misclassification of these has the potential to
565 become a systemic error if edge pixels were preferentially placed in a particular category. We assessed this error's
566 impact by taking high resolution IceBridge imagery (0.1m), downsampling to progressively lower resolution, and
567 reprocessing. Figure 11 shows the surface type percentages for three IceBridge images at decreasing resolution. Figure
568 12 shows a series of downsampled images and their classified counterparts. Surprisingly, despite clear pixilation and
569 aliasing in the imagery, little change in aggregate classification statistics occurred as resolution was lowered from 0.1
570 to 2m. This suggests that at resolutions used for this paper, edge pixels do not significantly impact the classification
571 results. It may also be possible to forego the pansharpening process discussed in section 3.1, and use 2m multispectral
572 WorldView imagery directly.

573 The second type of external error occurs when the human expert fails to correctly label a segment. Even skilled
574 human observers cannot classify every pixel in the imagery definitively, and indeed the division between the surface
575 types can sometimes be indistinct even to an observer on the ground. We addressed this concern by employing
576 observers extensively trained in the sea ice field, both in remote sensing and in-situ observations, comparing multiple
577 human classifications of the same segments. After discussion, the portion of image objects subject to human observer
578 disagreement or uncertainty is small. Human observers disagreed on 3% of objects creating our training sets. The
579 possibility of systemic bias among the expert observer classifications cannot be excluded because real ground truth,
580 in the form of geo-referenced ground observations from knowledgeable observers was, unfortunately, not available
581 for any of the imagery. Conducting this type of validation would be helpful, but given high confidence human expert
582 classifiers expressed in their classifications and low disagreement between them, may not be essential.

Deleted: Segmentation error, the

Deleted: ,

Deleted: caused when

586 **5.1.3 Overall Error**

587 The fact that misclassification dominates the internal error metric suggests that error could be reduced if additional
588 object attributes used by human experts to differentiate surface types could be identified. The agreement between the
589 OSSP method and a human (96%+/-3%) is similar to the agreement between different human observers (97%),
590 meaning that the algorithm is nearly as accurate as a human manually classifying an entire image. If we exclude the
591 possibility for systemic error in human classification, and assume other errors are unrelated to one another, we can
592 calculate a total absolute accuracy in surface type determination as approximately 96%.

593 **5.2 Producing Derived Metrics of Surface Coverage**

594 The classified imagery, presented as a raster, (e.g. Fig. 7) is not likely to be the end product used in many analyses.
595 Metrics of the sea ice state in simpler form will be calculated. We already introduced the most basic summary metrics
596 in section 4, where we presented fractional surface coverage calculated from the total pixel counts for each of the four
597 surface categories in each image. We also presented the calculation of melt pond coverage as a fraction of the ice-
598 covered portion of the image, rather than total image area. The calculation of these is straightforward. Other metrics
599 commonly discussed in the literature that could be produced with minimal additional processing include those
600 capturing melt pond size, connectivity, or fractal dimension, as well as floe size distribution or perimeter to area ratio.
601 As with definitions of surface type, standardizing metrics will be necessary to produce intercomparable results. We
602 discussed the more complex metrics which could be derived from this imagery with several other groups. We
603 determined that standardizing these and other more advanced metrics will require more input and consensus building
604 before a community standard can be suggested. We leave determining standard methods for calculating these more
605 complex metrics to a future work.

606 Equipped with the images processed by OSSP, we consider what size area must be imaged, classified, and
607 summarized to constitute 'one observation' and how regionally representative such an observation is. Even with the
608 increasing availability of high resolution imagery, it is unlikely that high resolution imaging will regularly cover more
609 than a small portion of the Arctic in the near future. As a result, high resolution image analysis will likely remain a
610 'sampling' technique. Since the scale of sea ice heterogeneity varies for each property type, a minimum area unique
611 to that property must be analyzed to qualify as a representative sample of the surface conditions. Finding that minimum
612 area involves addressing the 'aggregate scale' – the area over which a measured surface characteristic becomes
613 uniform and captures a representative average of the property in the area (Perovich, 2005). It may also be possible to
614 determine an aggregate scale statistic within well constrained bounds by random sub-sampling of the region, and
615 therefore reduce processing time. Here we conduct analysis of these sampling concepts and suggest this analysis of
616 the aggregate scale be conducted for any metric.

617 First, we sought to determine the aggregate scale for the simple fractional coverage metrics of ice as a fraction of
618 total area and melt pond as a fraction of ice area. This would inform us, for example, as to whether processing the
619 entire area of a WorldView image (up to 1000km²) was necessary, or alternatively if a full WorldView image was
620 sufficient to constitute a sample. First, we evaluated the convergence of fractional coverage within areas of increasing
621 size towards the image mean. For a WorldView image depicting primarily first year ice in various stages of melt, we

- Deleted:** ;
- Deleted:** ; and ridged ice coverage or frequency
- Deleted:** For this general work
- Deleted:** felt that more important than the specific definition of additional metrics of surface heterogeneity, is the consideration of what
- Deleted:** for
- Deleted:** to be collected
- Deleted:** Similarly, it
- Deleted:** sub-sample within a representative area and
- Deleted:** the mean of
- Deleted:** sample
- Deleted:** , reducing
- Deleted:** this area
- Deleted:** Equipped with the images processed by OSSP
- Deleted:** first
- Deleted:** for ice
- Deleted:** coverage (
- Deleted:**).
- Deleted:** worldview
- Deleted:** (~
- Deleted:** worldview
- Deleted:** We did this by evaluating
- Deleted:** feature
- Deleted:** image
- Deleted:** to a regional
- Deleted:** each
- Deleted:** acquired during the melt season, we determined the fractional
- Deleted:** pond and ice coverage within

652 created non-overlapping gridded subsections, and determined the fractional coverage within each grid cell. The size of
653 grid cells was varied logarithmically from 100 x 100 pixels (10^2) to 31622x31622 pixels ($10^{4.5}$) or from 0.0025km² to
654 250km². For each sample size, we gridded the image and evaluated every subsection within the entire image. Figure
655 13a shows a scatterplot of the fractional melt pond coverage in each image grid plotted against the log of total area of
656 that grid cell. As the area sampled increases, the melt pond fraction shows lower deviation from the mean, as expected.
657 To assist in evaluating the convergence towards the mean, we plot the 95% prediction interval for each image subset
658 size in Fig. 13a (large red dots). The range of pond fraction values between these two points represents the interval
659 within which 95% of samples of this size would fall. The width of the 95% prediction interval declines linearly with
660 respect to sample area in log space, shrinking by 0.3 for each order of magnitude that sample area increases. Visually
661 it appears that maximum convergence may have been reached at a sample area of ~30km² (~10^{1.5}km²), though there
662 are an insufficient number of samples at this large area within a single image to be certain. Regardless of whether
663 convergence is complete, the prediction interval tells us that at 30km², 95% of areas sampled could be expected to
664 have pond coverage within 5% of the mean of a full image (~1000km²). This is consistent with prior work that
665 indicated the aggregate scale for melt pond fraction determination is on the order of several tens of square kilometers
666 (Perovich, 2005; Perovich et al., 2002a). In Fig. 13b we conduct the same analysis for the total ice-covered fraction
667 (ponded + unponded ice) of the image. We see the range of the prediction interval generally drops as larger samples
668 are taken, but does not converge as cleanly or quickly as the pond coverage prediction interval does - a finding that is
669 unsurprising as ice fraction is composed of discrete floes with sizes much larger than melt ponds. The limited
670 convergence indicates that the aggregate scale for determination of ice covered fraction is at least on the order of the
671 scale of a WorldView image, and likely larger. Aggregate scale ice concentration, unlike melt pond fraction, is a
672 statistic better observed with medium resolution remote sensing platforms such as MODIS or Landsat due to the need
673 for a larger satellite footprint. WorldView imagery may be particularly useful for determining smaller scale parts of
674 floe size distributions or for validating larger scale remote sensing of ice fraction, if the larger scale pixels can be
675 completely contained within the worldview image. Floe size distribution will likely require nesting of scales in order
676 to fully access both large and small-scale parts of the floe size distribution.

677 We next investigated whether it is possible to reduce the processing load required to determine the melt pond or
678 ice fraction of an image within certain error bounds by processing collections of random image subsets. To do this, it
679 is useful to first establish two definitions: (1) one random sample of size N represents N randomly selected 100×100
680 pixel boxes, and (2) one adjacent sample of size N is a single area with size $100\sqrt{N} \times 100\sqrt{N}$. In other words, a
681 random sample and an adjacent sample both represent an image area of $10,000 * N$ pixels, but consist of independent
682 and correlated pixels, respectively. We expect random samples to better represent the total image mean melt pond
683 fraction because ice conditions are spatially correlated and a single large area is not composed of independent samples.
684 We evaluated this hypothesis by collecting 1000 random and adjacent samples of size $N=100$, with replacement.
685 Results are shown in Fig. 14. In Figure 14a, we plot a histogram of the mean melt pond fraction determined from these
686 1000 samples. The means determined from sets that contained randomly distributed image areas, are in red. The means
687 determined from sets of adjacent image areas are in blue. Although both sets represent samples of the same total image

- Deleted:** .
- Deleted:** subsections
- Deleted:** subsample
- Deleted:** for fractional surface coverage.
- Deleted:** 10
- Deleted:** determined from
- Deleted:** subset
- Deleted:** ice and pond
- Deleted:** in the image subset.
- Deleted:** determined from independent sample areas within the overall image
- Deleted:** toward
- Deleted:** size
- Deleted:** with a slope of approximately 0.3 across most of the range in sample area size explored. In other words, the prediction interval declines in width
- Deleted:** the
- Deleted:** is increased by. It
- Deleted:** or nearly reached
- Deleted:** we have
- Deleted:** size
- Deleted:** this
- Deleted:** scale
- Deleted:** image
- Deleted:** , and indicates that imagery representing an area as little as 3% of a Worldview image can provide an estimate of melt pond fraction that is representative of the mean at 1000km² scale within what may be tolerable limits for many applications. In Fig. 13b we conduct the same analysis, only this time for
- Deleted:** since the
- Deleted:** (We limit prediction interval to the range 0-1.)
- Deleted:** further
- Deleted:** in
- Deleted:** case, the idea
- Deleted:** collect a large number of
- Deleted:** of from an image, instead of a single, larger sample of the same area as the sum of the smaller random samples. We expected the random samples will
- Deleted:** overall
- Deleted:** the
- Deleted:** larger
- Deleted:** Namely, ice conditions are spatially correlated.
- Deleted:** processing sets of 100 image subsamples representing both adjacent and randomly selected image areas.
- Deleted:** 1000 sets of image areas. Each of the sets contained 100 sample areas of 100x100 pixels. The means determined from sets that contained adjacent image areas, essentially representing a single image sample 10 times larger in area, are in blue.
- Deleted:** selected
- Deleted:** Though

738 area, the one composed of independent subsets randomly selected from across the image does a much better job of
739 representing the mean value, with a smaller standard deviation.

740 Estimating the mean of a complete image by sampling randomly selected areas of the image becomes a simple
741 statistics problem. The sample size needed to estimate a population mean to within a certain confidence interval and
742 margin of error can be determined with the formula:

743
$$n = \left(\frac{Z\sigma}{ME} \right)^2$$

744 where n is the sample size, Z is the z-score for the confidence interval required, σ is the population standard deviation,
745 and ME is the margin of error. The standard deviation of random samples with size 100 is ~0.2 (Fig 14b). Assuming
746 a 95% confidence interval (Z=1.96), and a margin of error of 5%, a sample size of 64 is required. In other words, with
747 64 random samples of size 100 we can predict the mean melt pond fraction of the total image with 95% confidence to
748 within 5%. 64 samples of size 100 corresponds to an image area of ~16km², significantly smaller than the total image
749 size.

750 In order to show these results visually, we return to Fig. 13 and place another set of 95% prediction interval bounds
751 (purple dots). These bounds represent the prediction interval for a random sample of size necessary for the total area
752 to equal the area on the x axis. The result is quite powerful. By processing as little as 16km² of the image, collected
753 from samples randomly distributed across the area, we can determine aggregate melt pond fraction to within 5% of
754 the true value with a confidence of 95%. We estimate that this 5% margin of error is comparable to the sum of internal
755 (2-4%) and external errors in our processing algorithm (section 5.1). For large scale processing we suggest that when
756 the sample confidence interval is below the image processing technique accuracy, sampling of larger areas is no longer
757 necessary.

758 A similar analysis is presented in Fig. 14c and 14d for ice fraction. While the WorldView image is likely not large
759 enough to represent the aggregate scale for ice fraction, randomly sampling the image still provides an expedient way
760 to determine the mean ice fraction of the image within certain bounds, while processing only a small fraction of the
761 image. Calculating the 95% prediction interval of random samples representing the total image area shown on the x
762 axis (purple dots) again shows that the total image mean can be estimated by calculating only a small portion of the
763 total image.

764 These explorations of image sampling permit us to recommend that users can estimate the total image pond fraction
765 by selecting N sets of 100 randomly selected 50x50m regions (where N is selected to provide the desired confidence
766 interval and margin of error). We suggest a standard, which incorporates some 'safety factor', for processing imagery
767 to produce estimates of melt pond fraction should be to process 25km² of area contained in at least 100 randomly
768 located image subsets from domains of at least 100km². We note that flying a UAV over a domain and collecting
769 imagery along flight tracks will not count as fully 'random' in this context, since the images along-track are spatially
770 correlated. Since an image does not represent the aggregate scale for ice fraction, we cannot recommend a specific
771 sampling strategy for the aggregate scale, but note that processing of 25km² of imagery from randomly distributed
772 subsets produces a prediction interval around the mean of approximately the same size as the upper limit of uncertainty
773 for our image processing technique. The statistical approach for determining aggregate statistics should not depend

Deleted: Figure 14b shows the standard deviation for the same image sets. Independent samples from across the image show a lower range in lower standard deviation within the image sets as well, though the average standard deviation is slightly higher. Again, this is expected, given the strong spatial correlation of surface coverage fraction within the images

Deleted: We next test the central limit theorem to see how well we can predict the error bounds from processing a single set of independent (i.e. randomly distributed) samples. The central limit theorem states that when taking the mean of a sufficiently large number of independent samples of a random variable, the standard error of the mean of the samples is equal to $\frac{\sigma}{\sqrt{N}}$ where σ is the standard deviation of the sample values and N is the sample size. The standard deviation of pond coverage fraction in sets of 100 sub-images ranged from 0.15 to 0.25 across the 1000 sample sets run (see histogram in Fig. 14b) This yields a predicted standard error of the mean determined from any one of these sets of 0.015 to 0 (... [1])

Deleted: Fig. 13

Deleted: now

Deleted: , this time representing twice the standard error (... [2])

Deleted: 100 randomly distributed sub-areas that total

Deleted: We show that

Deleted: a relatively small fraction

Deleted: area, so long as that sub-area is

Deleted: a large number of

Deleted: permits expedient determination of melt pond frac (... [3])

Deleted: scale. In this case, processing as little as 5km² (~0 (... [4])

Deleted: determined for the entire image. We estimate that

Deleted: determined melt pond fraction is

Deleted: reasonable

Deleted: of

Deleted: .

Deleted: .

Deleted: 95% prediction

Deleted: (sampling error)

Deleted: well

Deleted: worthwhile

Deleted: A test of the central value theorem again shows th (... [5])

Deleted: that can be expected for image sets containing 100

Deleted: that

Deleted: the

Deleted: , with some safety factor built in,

Deleted: must process imagery representing at least 5km² if (... [6])

Deleted: located subsets from domains of at least 30 km²

Deleted: produce an 'aggregate scale' estimate

Deleted: pond coverage.

Deleted: 10km²

Deleted: 5km²

Deleted: 100

Deleted: These

854 [on the seasonality of the image nor the type of image used so long as the total area observed is sufficiently greater](#)
855 [than the variability in the surface feature being investigated. However, these](#) recommendations should be considered
856 provisional, because they are subject to impacts from differences in ice property correlation scales, and should be
857 further evaluated for accuracy as larger processed datasets are available.

858 5.3 Community Adoption

859 We have provided a free distribution of the OSSP algorithm and the training sets discussed in section 3.4 and 4 as a
860 companion to this publication, complete with detailed startup guides and documentation. This OSSP algorithm has
861 been implemented entirely in Python using open source resources with release to additional users in mind. The code,
862 along with documentation, instructional guidelines, and premade training sets (those used for the analyses herein) is
863 available at <https://github.com/wrightni/ossip> ([doi:10.5281/zenodo.1133689](https://doi.org/10.5281/zenodo.1133689)). The software is packaged with default
864 parameters and version controlled training sets for 4 different imagery sources. The package includes a graphical user
865 interface to allow users to build custom training datasets that suit their individual needs. The algorithm was constructed
866 with the flexibility to allow for the classification of any number of features given an appropriate training dataset.

867 Our intention is that by providing easy access to the code in an open source format, we will enable both specific
868 inquiries and larger scale image processing that supports community efforts at general sea ice monitoring. We plan to
869 continue improving and updating the code as it gains users and we receive community feedback. We hope to encourage
870 others to design their own features and add-ons. Since the predictive ability of the machine learning algorithm
871 improves as more training data is added, we wish to strongly encourage the use of the GUI to produce additional
872 training sets and we plan to collate other users training sets into improved training versions. See documentation of the
873 training set creation GUI for more information on how to share a training set.

874 The OSSP algorithm helps to bring the goal of having a standardized method for deriving geophysical parameters
875 from high resolution optical sea ice imagery closer to reality. In the larger picture, developing such a tool is only the
876 first step. We recall that the motivation behind this development was the need to quantify sea ice surface conditions
877 in a way that could enable better understanding of the processes driving changes in sea ice cover. The value of the
878 toolkit will only be realized if it is used for these scientific inquiries. We look forward to working with imagery owners
879 to facilitate processing of additional datasets.

880 6. Conclusions

881 We have implemented a method for classifying the sea ice surface conditions from high resolution optical imagery of
882 sea ice. We designed the system to have a low barrier to entry, by coding it in an open source format, providing
883 detailed documentation, and releasing it publicly for community use. The code identifies the dominant surface types
884 found in sea ice imagery; open water, melt ponds, [and submerged ice, and snow](#) and ice, with accuracy that averages
885 96 percent – comparable to the consistency between manual expert human classifications of the imagery. The
886 algorithm is shown to be capable of classifying imagery from a range of image sensing platforms including
887 panchromatic and pansharpened WorldView satellite imagery, aerial sRGB imagery, and optical DMS imagery from

Deleted: .

Deleted: .

890 NASA IceBridge missions. Furthermore, the software can process imagery collected across the seasonal evolution of
891 the sea ice from early spring through complete ice melt, demonstrating it is robust even as the characteristics of the
892 ice features seasonally evolve. We conclude, based on our error analysis, that this automatic image processing method
893 can be used with confidence in analyzing the melt pond evolution at remote sites.

894 With appropriate processing, high resolution imagery collections should be a powerful tool for standardized and
895 routine observation of sea ice surface characteristics. We hope that providing easy access to the methods and algorithm
896 developed herein, we will facilitate the sea ice community convergence on a standardized method for processing high
897 resolution optical imagery either by adoption of this method, or by suggestion of an alternate method complete with
898 code release and error analysis.

900 The authors declare that they have no conflict of interest.

901
902 *Data Availability.* The OSSP algorithm code is available from <https://github.com/wrightni/oss>
903 <https://doi.org/10.5281/zenodo.1133689>. Image data and processing results are available at the NSF Arctic Data Center (ADC).
904 Raw and preprocessed image data from DigitalGlobe WorldView images are not available due to copyright, but can
905 be acquired from DigitalGlobe or the Polar Geospatial Center at the University of Minnesota.

906
907 *Acknowledgements.* This work was supported by the Office of Naval Research Award N0001413MP20144 and the
908 National Science Foundation Award PLR-1417436. We would like to thank Donald Perovich and Alexandra Arntsen
909 for their assistance in creating machine learning training datasets. We would also like to thank Arnold Song, Justin
910 Chen, and Elias Deeb for their assistance and guidance with the development of the OSSP code. WorldView satellite
911 imagery was provided with the DigitalGlobe NextView License through the University of Minnesota Polar Geospatial
912 Center. A collection of the aerial imagery was collected by the SIZONet project. Some data used in this paper were
913 acquired by [the NASA Operation IceBridge Project](#).

914 References

- 915 [Arntsen, A. E., Song, A. J., Perovich, D. K. and Richter-Menge, J. A.: Observations of the summer breakup of an](#)
916 [Arctic sea ice cover, *Geophys. Res. Lett.*, 42\(19\), 8057–8063, doi:10.1002/2015GL065224, 2015.](#)
- 917 Blaschke, T.: Object based image analysis for remote sensing, *ISPRS J. Photogramm. Remote Sens.*, 65(1), 2–16,
918 doi:10.1016/j.isprsjprs.2009.06.004, 2010.
- 919 Blaschke, T., Hay, G. J., Kelly, M., Lang, S., Hofmann, P., Addink, E., Queiroz Feitosa, R., van der Meer, F., van der
920 Werff, H., van Coillie, F. and Tiede, D.: Geographic Object-Based Image Analysis – Towards a new paradigm,
921 *ISPRS J. Photogramm. Remote Sens.*, 87, 180–191, doi:10.1016/j.isprsjprs.2013.09.014, 2014.
- 922 Breiman, L.: Bagging Predictors, *Mach. Learn.*, 24(2), 123–140, doi:10.1023/A:1018054314350, 1996.
- 923 Breiman, L.: Random Forests, *Mach. Learn.*, 45(1), 5–32, doi:10.1023/A:1010933404324, 2001.

Deleted: during the review process, and will be transferred to a permanent repository for publication.

Deleted:), and a permanent DOI is pending.

Deleted: will

Deleted: be made

Deleted: for

Deleted: reasons

Deleted: NASA's

932 Curry, J. A., Schramm, J. L. and Ebert, E. E.: Sea ice-albedo climate feedback mechanism, *J. Clim.*, 8(2), 240–247,
933 doi:10.1175/1520-0442(1995)008<0240:SIACFM>2.0.CO;2, 1995.

934 DeFries, R. .: Multiple Criteria for Evaluating Machine Learning Algorithms for Land Cover Classification from
935 Satellite Data, *Remote Sens. Environ.*, 74(3), 503–515, doi:10.1016/S0034-4257(00)00142-5, 2000.

936 DeMott, P. J. and Hill, T. C. J.: Investigations of Spatial and Temporal Variability of Ocean and Ice Conditions in and
937 Near the Marginal Ice Zone. The “Marginal Ice Zone Observations and Processes Experiment” (MIZOPEX) Final
938 Campaign Summary, DOE ARM Climate Research Facility, Pacific Northwest National Laboratory; Richland,
939 Washington., 2016.

940 Dominguez, R.: IceBridge DMS L0 Raw Imagery, Version 1, , doi:10.5067/UMFN22VHGGMH, 2010.

941 Duro, D. C., Franklin, S. E. and Dubé, M. G.: A comparison of pixel-based and object-based image analysis with
942 selected machine learning algorithms for the classification of agricultural landscapes using SPOT-5 HRG imagery,
943 *Remote Sens. Environ.*, 118, 259–272, doi:10.1016/j.rse.2011.11.020, 2012.

944 Eicken, H.: Tracer studies of pathways and rates of meltwater transport through Arctic summer sea ice, *J. Geophys.*
945 *Res.*, 107(C10), 8046, doi:10.1029/2000JC000583, 2002.

946 [Fetterer, F. and Untersteiner, N.: Observations of melt ponds on Arctic sea ice, *J. Geophys. Res. Ocean.*, 103\(C11\),](#)
947 [24821–24835, doi:10.1029/98JC02034, 1998.](#)

948 GDAL: GDAL - Geospatial Data Abstraction Library, Version 2.1.0, Open Source Geospatial Found. [online]
949 Available from: <http://gdal.org>, 2016.

950 Inoue, J., Curry, J. A. and Maslanik, J. A.: Application of Aerosondes to Melt-Pond Observations over Arctic Sea Ice,
951 *J. Atmos. Ocean. Technol.*, 25(2), 327–334, doi:10.1175/2007JTECHA955.1, 2008.

952 Kurtz, N. T., Farrell, S. L., Studinger, M., Galin, N., Harbeck, J. P., Lindsay, R., Onana, V. D., Panzer, B. and Sonntag,
953 J. G.: Sea ice thickness, freeboard, and snow depth products from Operation IceBridge airborne data, *Cryosph.*,
954 7(4), 1035–1056, doi:10.5194/tc-7-1035-2013, 2013.

955 Kwok, R.: Declassified high-resolution visible imagery for Arctic sea ice investigations: An overview, *Remote Sens.*
956 *Environ.*, 142, 44–56, doi:10.1016/j.rse.2013.11.015, 2014.

957 Kwok, R. and Rothrock, D. A.: Decline in Arctic sea ice thickness from submarine and ICESat records: 1958-2008,
958 *Geophys. Res. Lett.*, 36(15), n/a-n/a, doi:10.1029/2009GL039035, 2009.

959 Landy, J., Ehn, J., Shields, M. and Barber, D.: Surface and melt pond evolution on landfast first-year sea ice in the
960 Canadian Arctic Archipelago, *J. Geophys. Res. Ocean.*, 119(5), 3054–3075, doi:10.1002/2013JC009617, 2014.

961 Laxon, S. W., Giles, K. A., Ridout, A. L., Wingham, D. J., Willatt, R., Cullen, R., Kwok, R., Schweiger, A., Zhang,
962 J., Haas, C., Hendricks, S., Krishfield, R., Kurtz, N., Farrell, S. and Davidson, M.: CryoSat-2 estimates of Arctic
963 sea ice thickness and volume, *Geophys. Res. Lett.*, 40(4), 732–737, doi:10.1002/grl.50193, 2013.

964 Lu, P., Li, Z., Cheng, B., Lei, R. and Zhang, R.: Sea ice surface features in Arctic summer 2008: Aerial observations,
965 *Remote Sens. Environ.*, 114(4), 693–699, doi:10.1016/j.rse.2009.11.009, 2010.

966 Markus, T., Cavalieri, D. J., Tschudi, M. A. and Ivanoff, A.: Comparison of aerial video and Landsat 7 data over
967 ponded sea ice, *Remote Sens. Environ.*, 86(4), 458–469, doi:10.1016/S0034-4257(03)00124-X, 2003.

968 Markus, T., Stroeve, J. C. and Miller, J.: Recent changes in Arctic sea ice melt onset, freezeup, and melt season length,
969 J. Geophys. Res., 114(C12), C12024, doi:10.1029/2009JC005436, 2009.

970 Maslanik, J., Stroeve, J., Fowler, C. and Emery, W.: Distribution and trends in Arctic sea ice age through spring 2011,
971 Geophys. Res. Lett., 38(13), doi:10.1029/2011GL047735, 2011.

972 Miao, X., Xie, H., Ackley, S. F., Perovich, D. K. and Ke, C.: Object-based detection of Arctic sea ice and melt ponds
973 using high spatial resolution aerial photographs, Cold Reg. Sci. Technol., 119, 211–222,
974 doi:10.1016/j.coldregions.2015.06.014, 2015.

975 [Miao, X., Xie, H., Ackley, S. F. and Zheng, S.: Object-Based Arctic Sea Ice Ridge Detection From High-Spatial-
976 Resolution Imagery, IEEE Geosci. Remote Sens. Lett., 13\(6\), 787–791, doi:10.1109/LGRS.2016.2544861, 2016.](#)

977 Pal, M.: Random forest classifier for remote sensing classification, Int. J. Remote Sens., 26(1), 217–222,
978 doi:10.1080/01431160412331269698, 2005.

979 Parkinson, C. L. and Comiso, J. C.: On the 2012 record low Arctic sea ice cover: Combined impact of preconditioning
980 and an August storm, Geophys. Res. Lett., 40(7), 1356–1361, doi:10.1002/grl.50349, 2013.

981 Pedregosa, F., Varoquaux, G., Gramfort, A., Michel, V., Thirion, B., Grisel, O., Blondel, M., Prettenhofer, P., Weiss,
982 R., Dubourg, V., Vanderplas, J., Passos, A., Cournapeau, D., Brucher, M., Perrot, M. and Duchesnay, É.: Scikit-
983 learn: Machine Learning in Python, J. Mach. Learn. Res., 12(Oct), 2825–2830 [online] Available from:
984 <http://jmlr.csail.mit.edu/papers/v12/pedregosa11a.html> (Accessed 24 July 2017), 2011.

985 Perovich, D. K.: On the aggregate-scale partitioning of solar radiation in Arctic sea ice during the Surface Heat Budget
986 of the Arctic Ocean (SHEBA) field experiment, J. Geophys. Res., 110(C3), C03002, doi:10.1029/2004JC002512,
987 2005.

988 Perovich, D. K., Tucker, W. B. and Liggett, K. A.: Aerial observations of the evolution of ice surface conditions during
989 summer, J. Geophys. Res., 107(C10), 8048, doi:10.1029/2000JC000449, 2002a.

990 Perovich, D. K., Grenfell, T. C., Light, B. and Hobbs, P. V.: Seasonal evolution of the albedo of multiyear Arctic sea
991 ice, J. Geophys. Res., 107(C10), 8044, doi:10.1029/2000JC000438, 2002b.

992 Perovich, D. K., Richter-Menge, J. A., Jones, K. F. and Light, B.: Sunlight, water, and ice: Extreme Arctic sea ice
993 melt during the summer of 2007, Geophys. Res. Lett., 35(11), L11501, doi:10.1029/2008GL034007, 2008.

994 Petty, A. A., Tsamados, M. C., Kurtz, N. T., Farrell, S. L., Newman, T., Harbeck, J. P., Feltham, D. L. and Richter-
995 Menge, J. A.: Characterizing Arctic sea ice topography using high-resolution IceBridge data, Cryosph., 10(3),
996 1161–1179, doi:10.5194/tc-10-1161-2016, 2016.

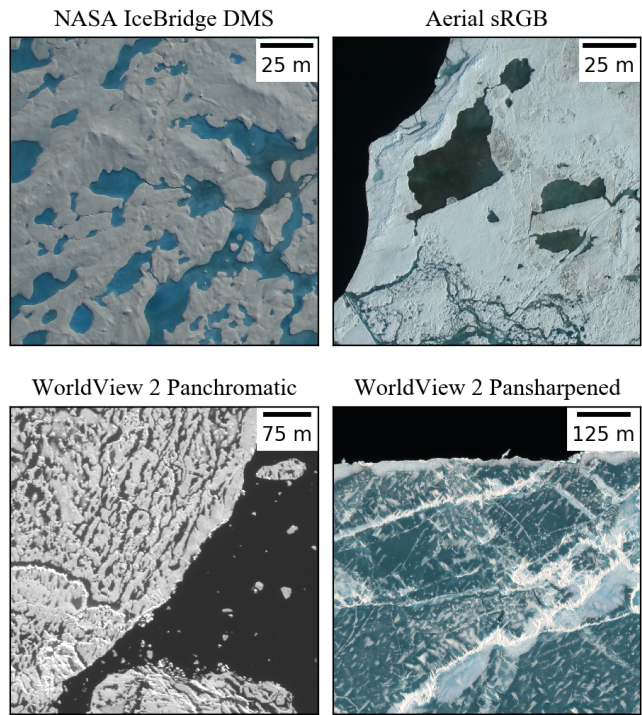
997 Pistone, K., Eisenman, I. and Ramanathan, V.: Observational determination of albedo decrease caused by vanishing
998 Arctic sea ice, Proc. Natl. Acad. Sci., 111(9), 3322–3326, doi:10.1073/pnas.1318201111, 2014.

999 Polashenski, C., Perovich, D. and Courville, Z.: The mechanisms of sea ice melt pond formation and evolution, J.
1000 Geophys. Res. Ocean., 117(C1), n/a-n/a, doi:10.1029/2011JC007231, 2012.

1001 Renner, A. H. H., Gerland, S., Haas, C., Spreen, G., Beckers, J. F., Hansen, E., Nicolaus, M. and Goodwin, H.:
1002 Evidence of Arctic sea ice thinning from direct observations, Geophys. Res. Lett., 41(14), 5029–5036,
1003 doi:10.1002/2014GL060369, 2014.

1004 Rösel, A. and Kaleschke, L.: Comparison of different retrieval techniques for melt ponds on Arctic sea ice from
1005 Landsat and MODIS satellite data, *Ann. Glaciol.*, 52(57), 185–191, doi:10.3189/172756411795931606, 2011.
1006 Rösel, A., Kaleschke, L. and Birnbaum, G.: Melt ponds on Arctic sea ice determined from MODIS satellite data using
1007 an artificial neural network, *Cryosph.*, 6(2), 431–446, doi:10.5194/tc-6-431-2012, 2012.
1008 Stroeve, J. C., Serreze, M. C., Holland, M. M., Kay, J. E., Malanik, J. and Barrett, A. P.: The Arctic’s rapidly shrinking
1009 sea ice cover: a research synthesis, *Clim. Change*, 110, 1005–1027, doi:10.1007/s10584-011-0101-1, 2012.
1010 Stroeve, J. C., Markus, T., Boisvert, L., Miller, J. and Barrett, A.: Changes in Arctic melt season and implications
1011 for sea ice loss, *Geophys. Res. Lett.*, 41, 1216–1225, doi:10.1002/2013GL058951. Received, 2014.
1012 Tschudi, M. A., Maslanik, J. A. and Perovich, D. K.: Derivation of melt pond coverage on Arctic sea ice using MODIS
1013 observations, *Remote Sens. Environ.*, 112(5), 2605–2614, doi:10.1016/j.rse.2007.12.009, 2008.
1014 van der Walt, S., Schönberger, J. L., Nunez-Iglesias, J., Boulogne, F., Warner, J. D., Yager, N., Gouillart, E. and Yu,
1015 T.: scikit-image: image processing in Python, *PeerJ*, 2, e453, doi:10.7717/peerj.453, 2014.
1016 Webster, M. A., Rigor, I. G., Perovich, D. K., Richter-menge, J. A., Polashenski, C. M. and Light, B.: Seasonal
1017 evolution of melt ponds on Arctic sea ice, *J. Geophys. Res. Ocean.*, 120(9), 1–15,
1018 doi:10.1002/2015JC011030. Received, 2015.
1019 Yan, G., Mas, J. -F., Maathuis, B. H. P., Xiangmin, Z. and Van Dijk, P. M.: Comparison of pixel-based and object-
1020 oriented image classification approaches—a case study in a coal fire area, Wuda, Inner Mongolia, China, *Int. J.*
1021 *Remote Sens.*, 27(18), 4039–4055, doi:10.1080/01431160600702632, 2006.

1022



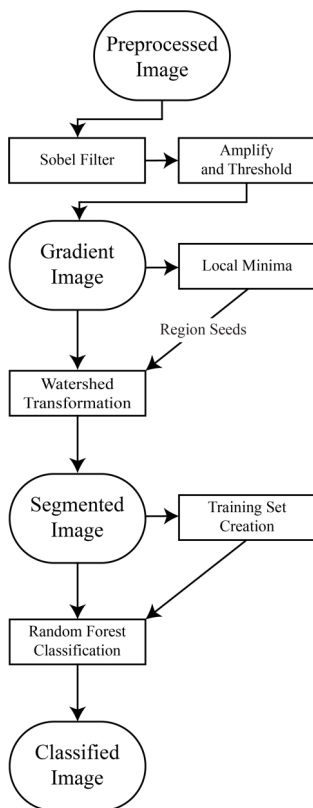
1024

1025

1026

Figure 1. Examples of imagery from each of the four imaging platforms that we seek to classify in this study. Each type of imagery has either a different spatial resolution or and different levels spectral information available.

- Deleted: types
- Deleted: process
- Deleted: Note the varying
- Deleted: sources, resolutions, and
- Deleted: for each image type

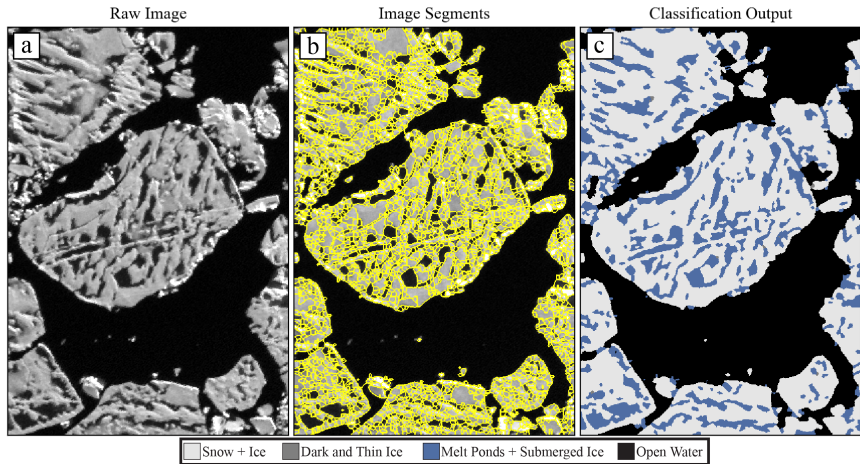


1032

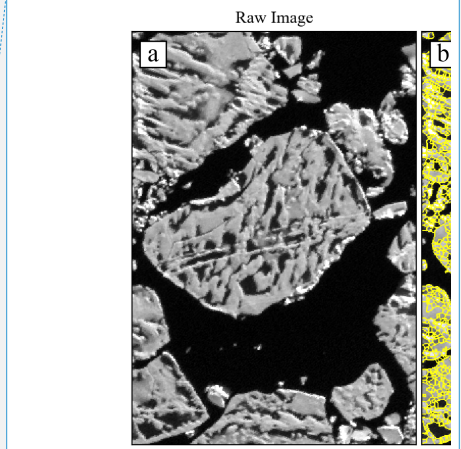
1033 **Figure 2.** Flow diagram depicting the steps taken to classify an image in the OSSP algorithm.

1034

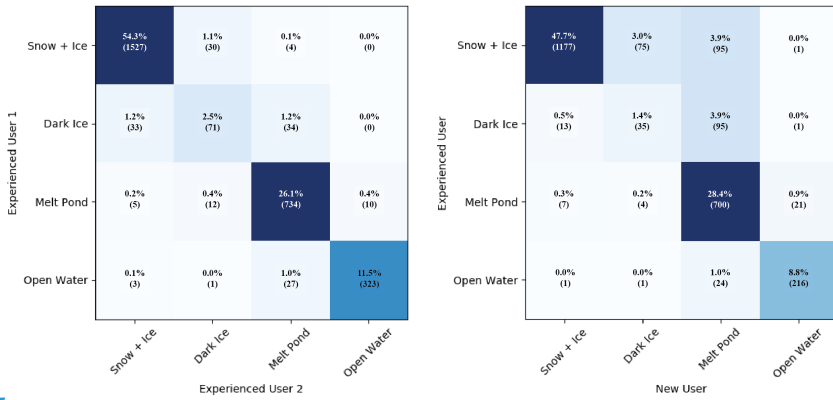
1035



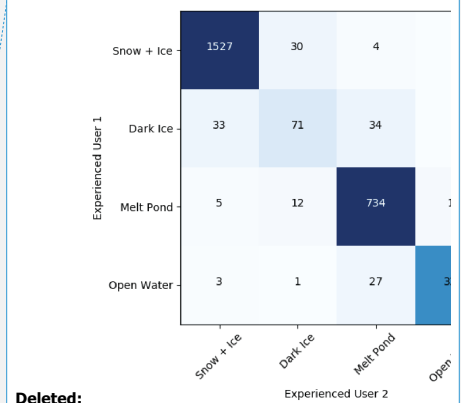
1036
1037
1038
1039
1040
1041
Figure 3. Visual representation of important steps in the image processing workflow. Panel (a) shows a section of a preprocessed panchromatic WorldView 2 satellite imagery, taken on July 1, 2014. In panel (b), outlines of the image objects created by our edge detection and watershed transformation are shown overlain on top of the image in panel (a). Panel (c) shows the result of replacing each object with a value corresponding to the prediction of the random forest classifier.



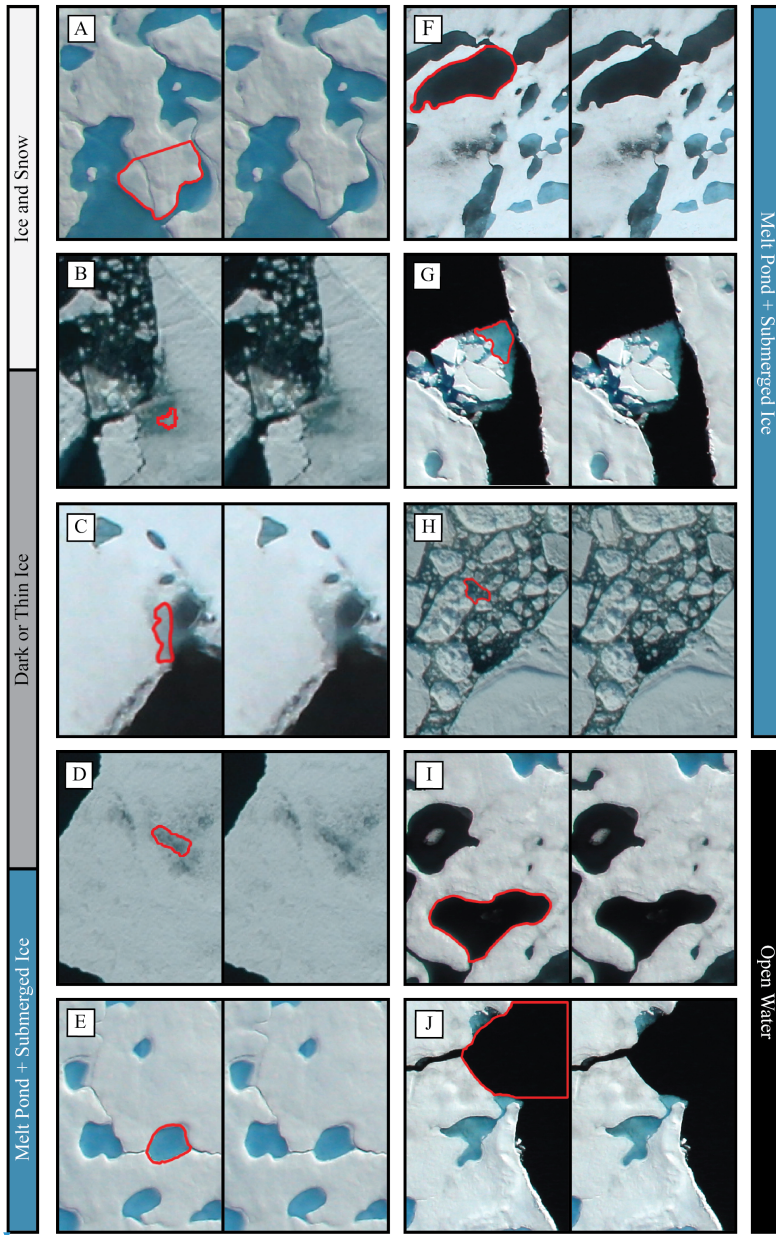
Deleted:
Deleted: Important...visual representation of important steps in the image processing workflow. Panel (a) shows a section of a preprocessed panchromatic WorldView 2 satellite image... imagery, taken on July 1, 2014. Panel...n panel (b) shows), outlines of the outline of ...image objects created from...y our edge detection and watershed transformation....are shown overlain on top of the image in panel (a). Panel (c) shows the classified ...result after running...f replacing each object through a



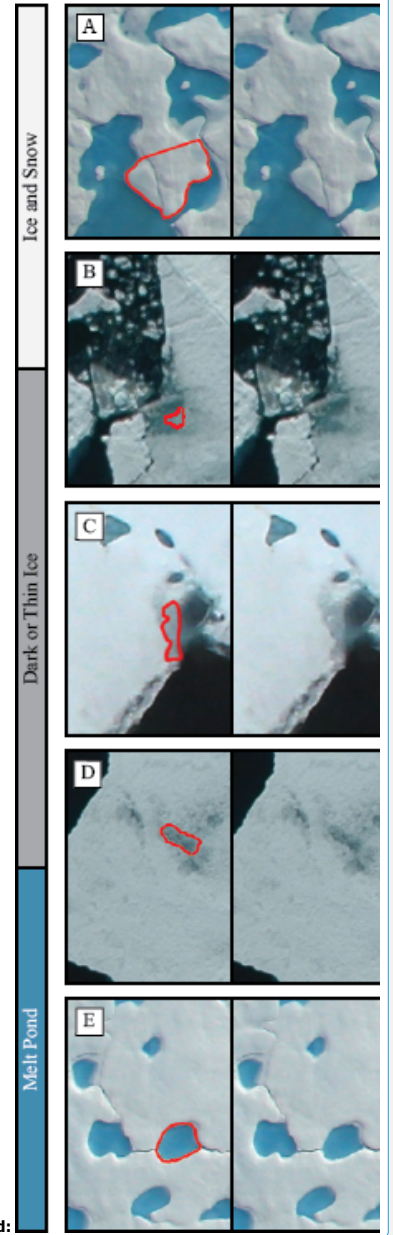
1042
1043
1044
1045
1046
Figure 4. Confusion matrices comparing classification tendencies between two users experienced with the image processing algorithm (left) and between an experienced user and a new user (right). Squares are colored based on the value of the cell, with darker colors indicating more matches. Values along the diagonal of each confusion matrix represents the agreement between each user, while values in off-diagonal regions represent disagreement.



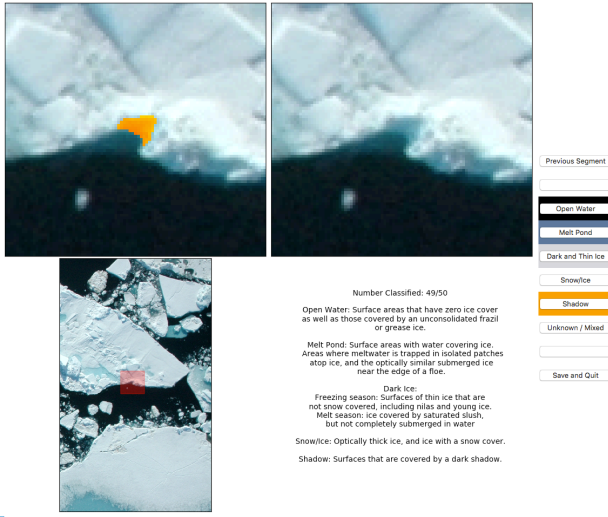
Deleted:
Deleted: patterns...endencies between two users experienced with the image processing algorithm (left) and between an experienced user and a new user (right). Squares are colored based on the number...alue of pixels in that...he cell, with darker colors indicating a larger number...ore matches. Values along the diagonal of pixels.



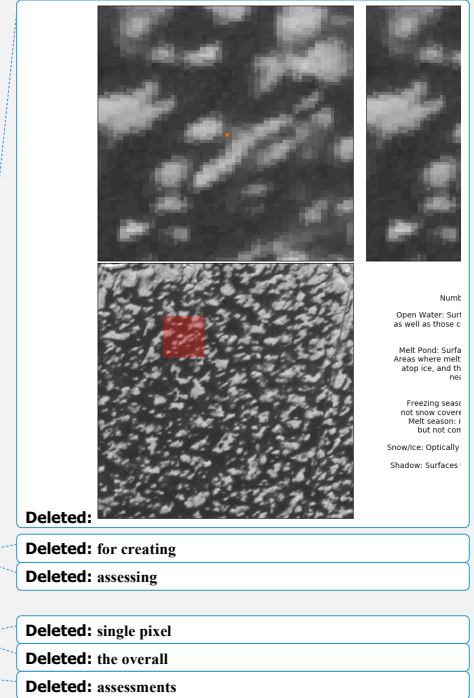
Deleted:

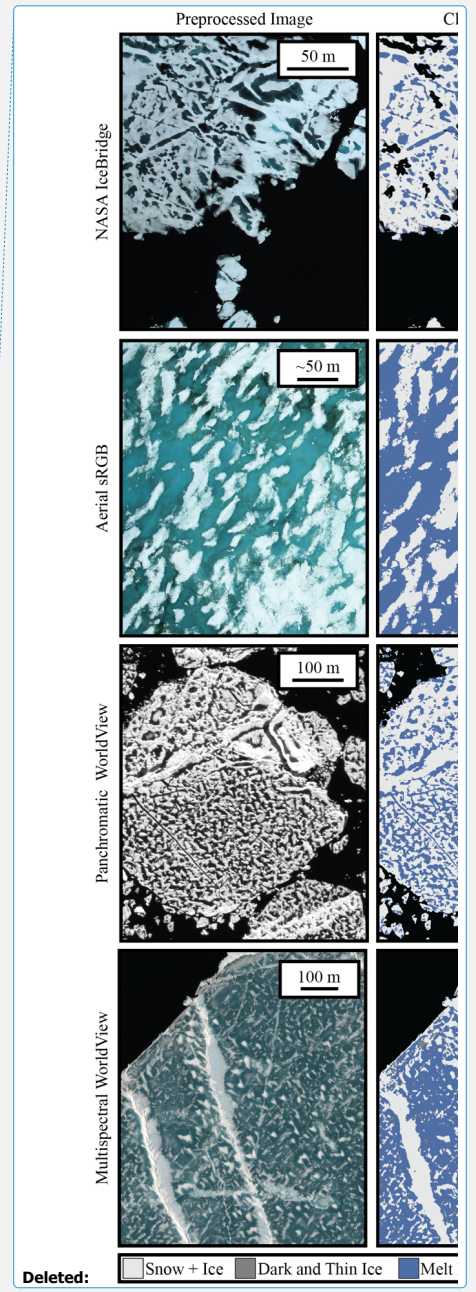
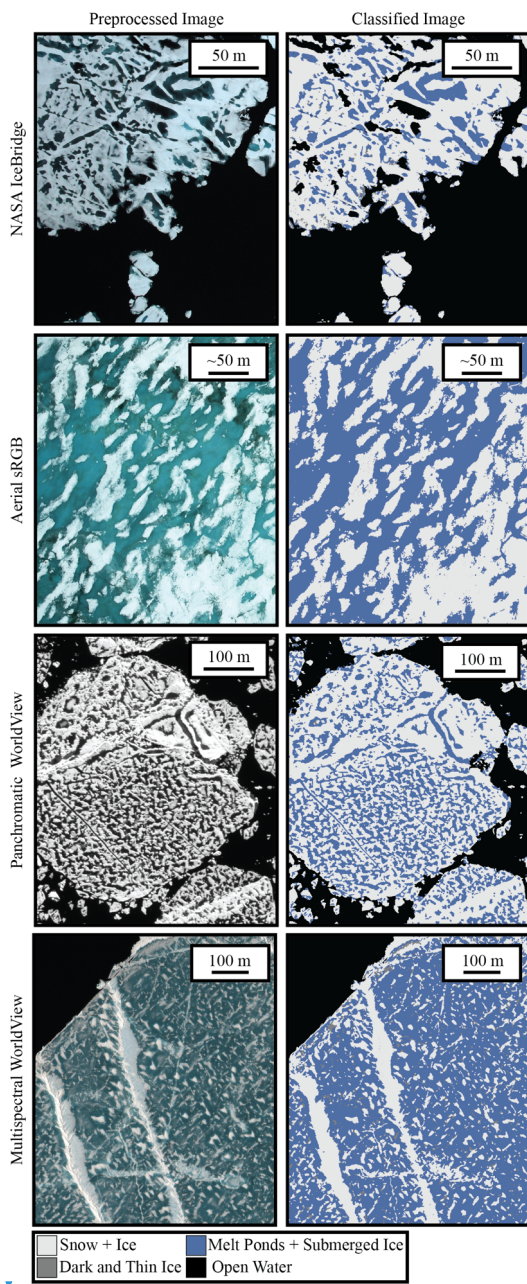


1085 Figure 5. Examples of surfaces seen in aerial imagery of sea ice that span our four classification categories. Panel A: snow
 1086 covered surface. Panel B: Ice with a thin surface scattering layer where disagreement on true classification exists -
 1087 represents a small fraction of total surface area. Panel C: Panel D: Surface transitioning to a melt pond that is not yet fully
 1088 submerged. Panel E: Melt pond. Panel F: Dark melt pond that has not completely melted through. Panel G: Submerged
 1089 ice. Panel H: Brush, mostly submerged, included in the melt pond category. Panel I: Melt pond that has completely melted
 1090 through to open water. Panel J: Open water.



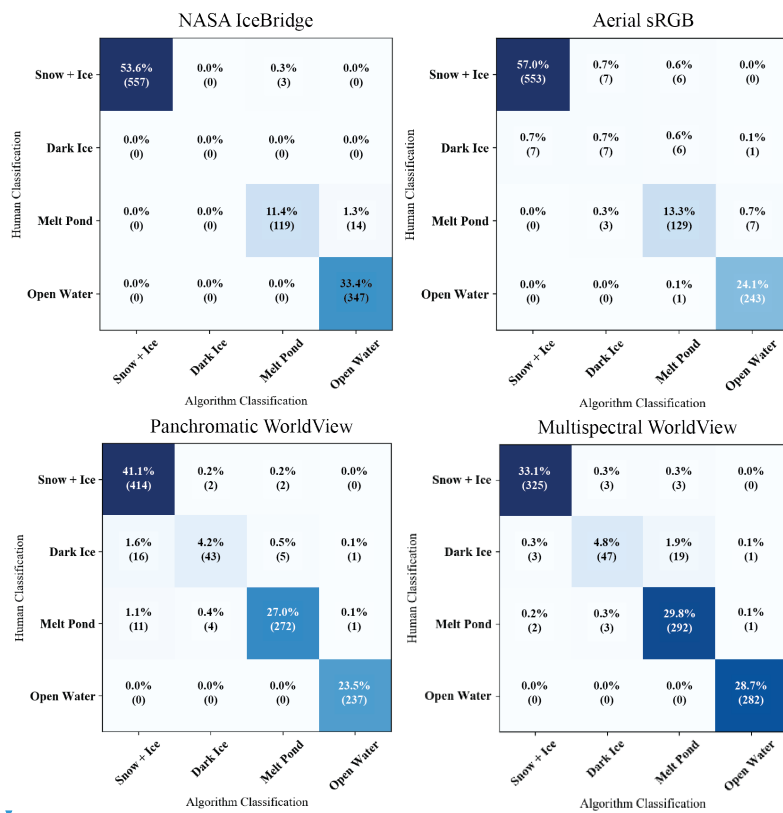
091
 092 **Figure 6. Graphical user interface used to create training datasets and to assess the accuracy of a classified image. Bottom**
 093 **left panel shows an overview of the region to provide the user with spatial context. Top left magnifies the image and**
 094 **highlights the segment of interest, while top right shows the same region with no segment overlap. The user is allowed to**
 095 **choose between any of the relevant surface categories, or to indicate that they are unsure of the classification. As shown,**
 096 **the user interface is demonstrating the classification of a segment for use in a training set. This same GUI is also capable of**
 097 **asking a user to classify an individual pixel, which can be compared to the final classified image for determining accuracy**
 098 **(section 3.6).**





108
109
110

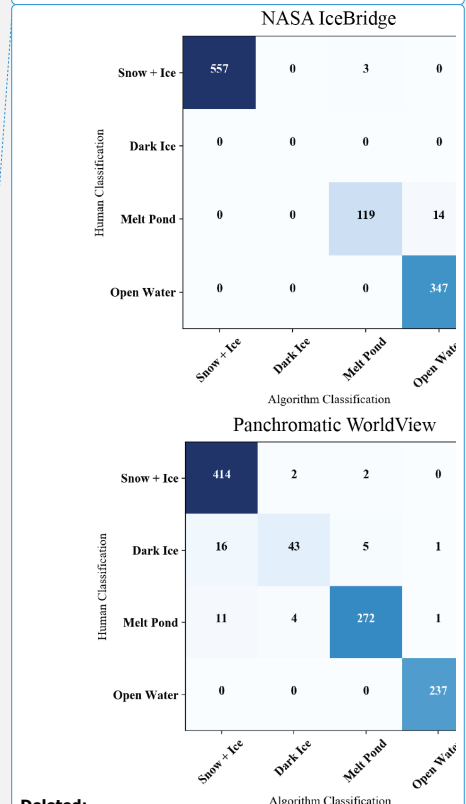
Figure 7. Side-by-side comparison of preprocessed imagery (left) and the result of classification (right) for each of the four imaging platforms. Images depict ice surfaces in varying stages of melt. The NASA IceBridge image, for example, is in very late stages of melt ponds that have already melted through to the ocean.



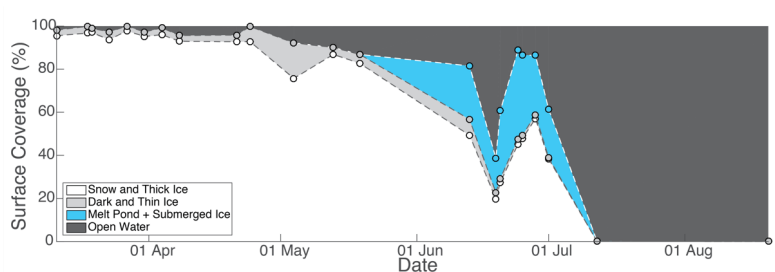
111
112
113
114
115

Figure 8. Accuracy confusion matrices comparing the classification of 1000-pixels between a human and the algorithm. Squares are colored based on the value of the cell, with darker colors indicating more matches. Values along the diagonal of each confusion matrix represents the agreement between each classifier, while values in off-diagonal regions represent disagreement.

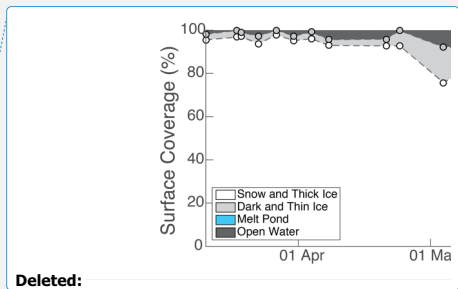
Deleted: classified
Deleted: . One scene was selected from each imagery source.
Deleted: imagery
Deleted: with many
Deleted: having



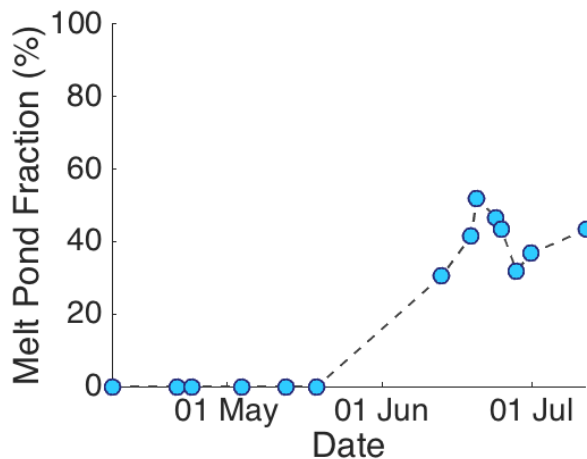
Deleted:
Deleted: 1000-pixel accuracy
Deleted: matrix for each image type.
Deleted: number
Deleted: pixels in that
Deleted: a larger number of pixels



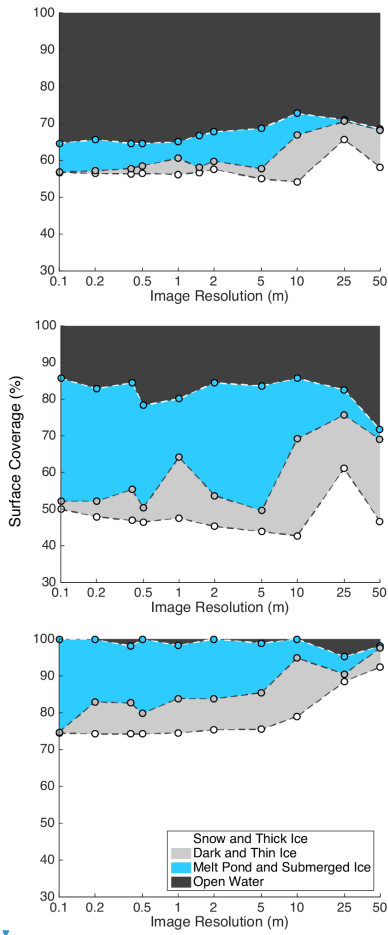
127
128 **Figure 9. Seasonal progression of surface type distributions at the satellite image collection site; 2014 in the Beaufort Sea**
129 **at 72°N 128°W. This site represents a Eulerian observation of the sea ice surface, and does not track a floe across its lifetime.**
130 **Average scene size was 956km² with a minimum of 304km² and a maximum of 1321km².**



Deleted:
Deleted: our

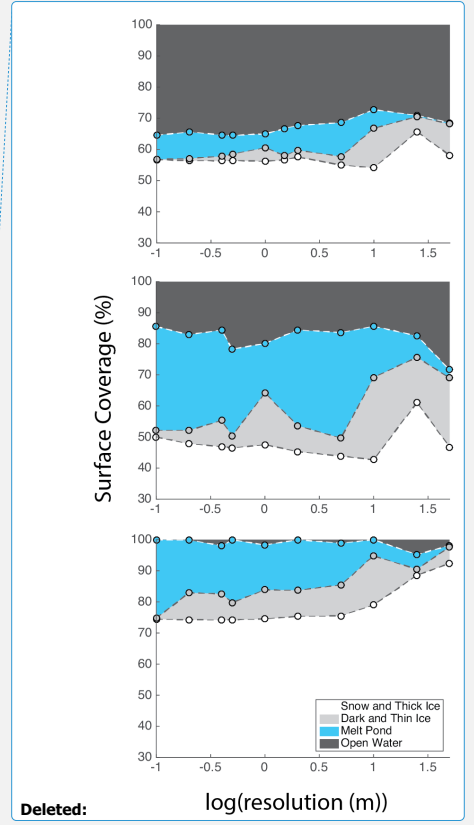


1132 **Figure 10. Evolution of melt pond fraction over the 2014 season at our satellite image collection site; 2014 in the Beaufort**
1133 **Sea at 72°N 128°W. This site represents a Eulerian observation of the sea ice surface, and does not track a floe across its**
1134 **lifetime. By August, the sea ice extent has retreated north of this location, and we therefore do not capture a full melt pond**
1135 **cycle.**



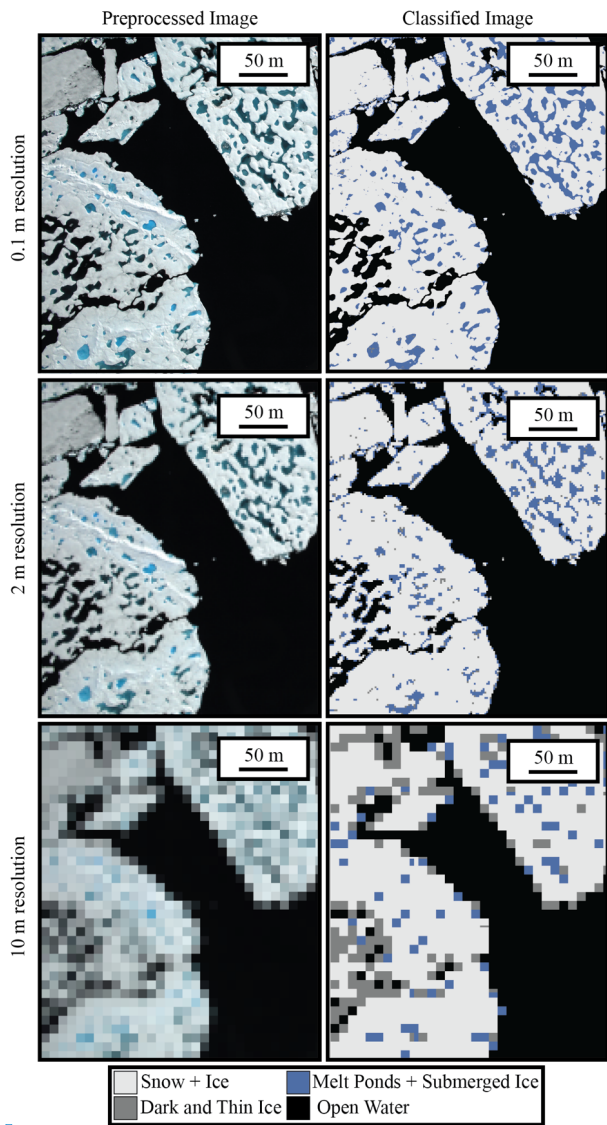
140
 141
 142
 143

Figure 11. Change in surface coverage percentage as a result of downsampling [three](#) IceBridge [images](#). Each plot represents a single image, with resolution along the x-axis on a log scale. Imagery starts at the nominal IceBridge resolution of 0.1m and is degraded to a maximum of 50m.



Deleted:

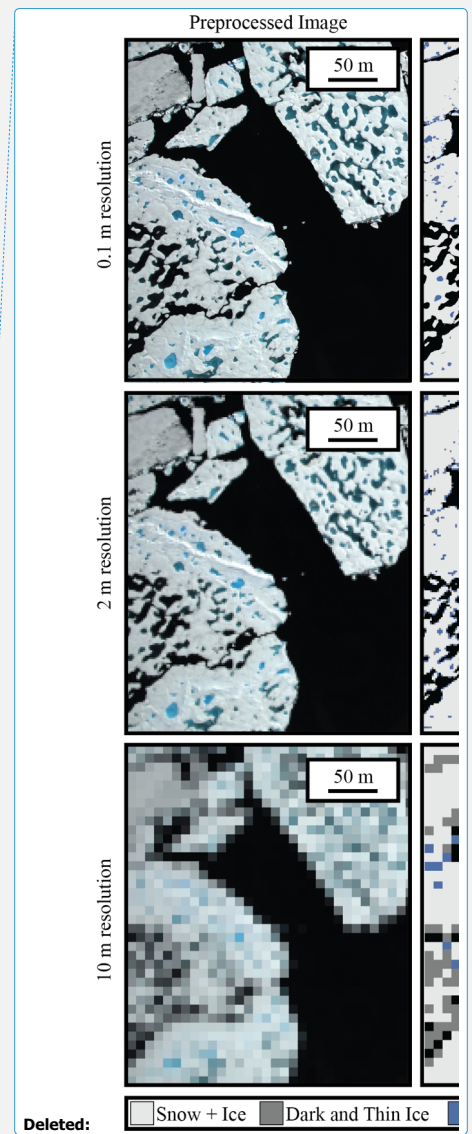
Deleted: imagery.



146

147 Figure 12. Visual demonstration of the downsampling effect on a [single](#) NASA IceBridge image. The top image is shown at
 148 the original 0.1 m resolution. The middle image is [a resolution of 2m](#) - the equivalent of a multispectral WorldView 2 image
 149 without pansharpening. [The bottom has a resolution of 10m](#), where pixel size has begun to exceed the average melt pond
 1150 size.

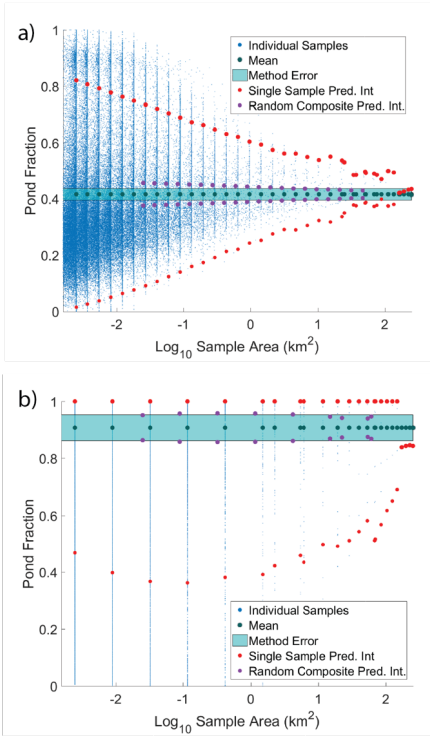
1151



Deleted: resolution

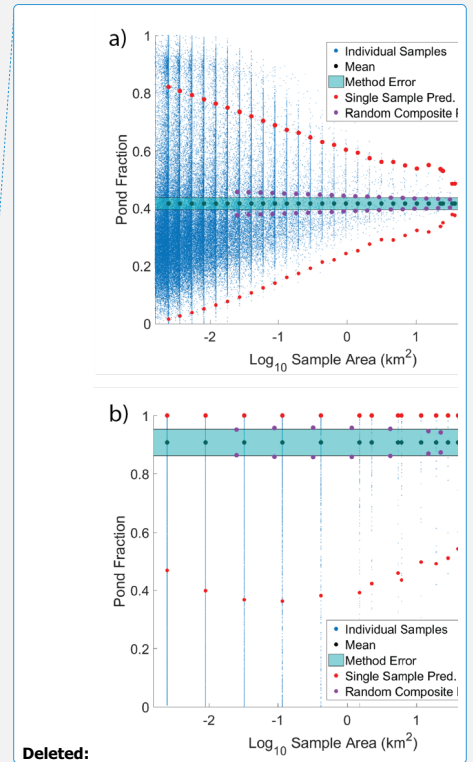
Deleted: In the

Deleted: image

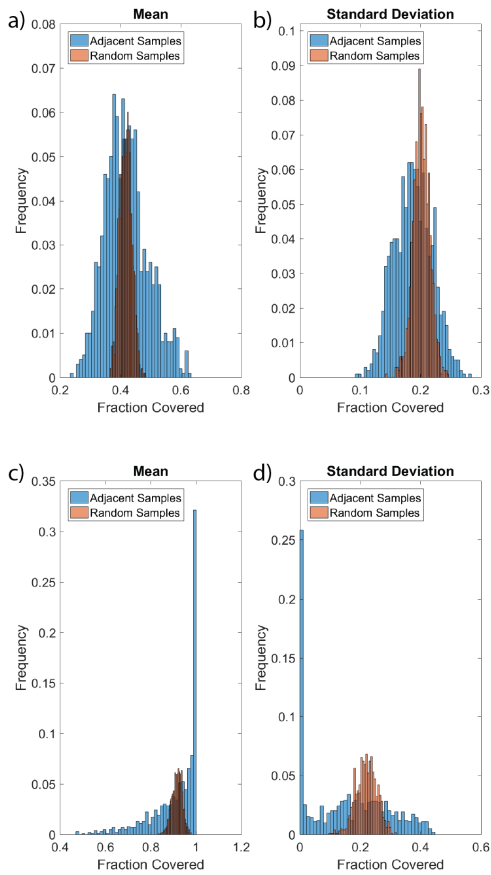


1156

1157 **Figure 13. Convergence of melt pond fraction (a) and ice fraction (b) for a WorldView image collected 25 June 2014 at 72°N**
 1158 **128°W as the area evaluated is increased. Small blue dots represent individual image subsets. For segments of a given size,**
 1159 **black dots represent the mean value of those samples, red dots represent the 95% prediction interval, and purple dots show**
 1160 **the 95% prediction interval for the same total area, but calculated from 100 randomly placed, smaller, samples. Cyan**
 1161 **shaded area represents the error in determination expected from the processing method.**



Deleted:



1163

1164 **Figure 14. Histogram of mean (a) and standard deviation (b) of 1000 melt pond fraction estimates, each calculated from**
 1165 **100 sample areas on a 25 June 2014 WorldView image. The 100 samples were either randomly distributed across the image**
 1166 **(red) or adjacent to each other (blue). Panels (c) and (d) show the same as (a) and (b), respectively, for ice fraction rather**
 1167 **than melt pond fraction.**

1168

1169

1170

1171

1172

1173

Attribute	MS	PAN	Aerial
Mean (Pan)			
Mean (Coastal)			
Mean (Blue)			
Mean (Green)			
Mean (Yellow)			
Mean (Red)			
Mean (Red Edge)			
Mean (NIR1)			
Mean (NIR2)			
Median (Pan)			
StDev (Pan)			
Min Intensity (Pan)			
Max Intensity (Pan)			
StDev (Blue)			
StDev (Green)			
StDev (Red)			
Entropy			
Segment Size			
Image Date			
Coastal / Green			
Blue / NIR1			
Green / NIR1			
Yellow / Red Edge			
Yellow / NIR1			
Yellow / NIR2			
Red / NIR1			
$(B1 - NIR1)/(B2 + NIR1)$			
$(G - R)/(G + R)$			
$(B - R)/(B + R)^1$			
$(B - G)/(B + G)^1$			
$(G - R)/(2*B - G - R)^1$			
Neighbor Mean			
Neighbor StDev			
Neighbor Max			
Neighbor Entropy			

1175 Miao et al. 2015

1176 Table 1. Attributes used for classifying each of the three image types. Blue squares indicate attributes that were used for
 1177 that image. Dark gray squares indicate attributes that are available, but were not found to be sufficiently beneficial in the
 1178 classification to merit inclusion under our criteria. Light gray squares indicate attribute that are not available on that image
 1179 type (e.g. band ratios on a panchromatic image). NIR is the near infrared wavelength. B1 is the costal WorldView band,
 1180 and B2 is the blue band. R, G, and B, stand for red, green, and blue, respectively.

- Deleted: , dark
- Deleted: are ones where the
- Deleted: is
- Deleted: are
- Deleted: wavelengths
- Deleted: B
- Deleted: G

Image ID	Sensor Type	Date Collected	Ice + Snow	DTI	MPS	OW	Accuracy
102001002C214D00	Panchromatic	11-Mar-14	96	3	0	2	97
103001002E8F0D00	Panchromatic	18-Mar-14	97	3	0	0	97
102001002BBA0C00	Panchromatic	19-Mar-14	97	2	0	1	96
103001002FC75200	Panchromatic	23-Mar-14	94	4	0	3	95
102001002CB77C00	Panchromatic	27-Mar-14	98	2	0	0	100
1030010030403A00	Panchromatic	31-Mar-14	95	2	0	3	98
1030010031B65000	Panchromatic	4-Apr-14	96	3	0	1	99
102001002BA6C100	Panchromatic	8-Apr-14	93	3	0	4	100
103001002F79A700	Panchromatic	21-Apr-14	93	3	0	4	98
1030010030371B00	Panchromatic	24-Apr-14	93	7	0	0	98
103001003102A600	Panchromatic	4-May-14	76	16	0	8	98
102001003007FA00	Panchromatic	13-May-14	87	3	0	10	97
10300100306F2E00	Panchromatic	19-May-14	83	4	0	13	96
102001003035D700	Panchromatic	13-Jun-14	49	7	25	18	95
1030010033AAC400	Panchromatic	19-Jun-14	20	3	16	61	97
1020010031DF9E00	Panchromatic	20-Jun-14	27	2	31	39	96
1020010032B94E00	Panchromatic	24-Jun-14	45	2	41	11	95
102001003122A700	Panchromatic	25-Jun-14	48	1	37	13	97
102001002F4F1A00	Panchromatic	28-Jun-14	57	2	28	14	95
10300100346D1200	Panchromatic	1-Jul-14	38	0	23	39	97
1030010035C8D000	Panchromatic	12-Jul-14	0	0	0	100	100
103001003421AB00	Panchromatic	20-Aug-14	0	0	0	100	100

Deleted: I+S

Deleted: MP

10300100324B7D00	Multispectral	13-Jun-14	44	7	29	19	96
1030010033AAC400	Multispectral	19-Jun-14	16	3	19	62	97
10300100346D1200	Multispectral	1-Jul-14	44	2	26	28	98
1030010035C8D000	Multispectral	12-Jul-14	0	0	0	100	100
2016_07_13_05863	IceBridge	13-Jul-16	50	2	34	14	92
2016_07_13_05882	IceBridge	13-Jul-16	72	1	26	0	97
2016_07_13_05996	IceBridge	13-Jul-16	70	2	28	0	95
2016_07_13_06018	IceBridge	13-Jul-16	61	2	36	1	91
2016_07_13_06087	IceBridge	13-Jul-16	66	1	33	0	99
2016_07_16_00373	IceBridge	16-Jul-16	9	0	2	89	100
2016_07_16_00385	IceBridge	16-Jul-16	66	1	14	20	98
2016_07_16_00662	IceBridge	16-Jul-16	49	1	16	35	98
2016_07_16_00739	IceBridge	16-Jul-16	67	2	25	6	97
2016_07_16_01569	IceBridge	16-Jul-16	22	0	7	71	97
2016_07_16_02654	IceBridge	16-Jul-16	35	0	10	54	95
2016_07_19_01172	IceBridge	19-Jul-16	62	0	14	24	90
2016_07_19_01179	IceBridge	19-Jul-16	57	0	10	32	95
2016_07_19_02599	IceBridge	19-Jul-16	51	0	7	43	99
2016_07_19_02603	IceBridge	19-Jul-16	69	0	9	22	99
2016_07_19_02735	IceBridge	19-Jul-16	74	0	25	0	100
2016_07_19_03299	IceBridge	19-Jul-16	57	0	8	35	96
2016_07_21_01221	IceBridge	21-Jul-16	49	0	4	47	97
2016_07_21_01311	IceBridge	21-Jul-16	87	1	5	7	95
2016_07_21_01316	IceBridge	21-Jul-16	92	0	4	4	99
DSC_0154	Aerial sRGB	8-Jun-09	43	4	53	0	94
DSC_0327	Aerial sRGB	8-Jun-09	33	3	63	0	90
DSC_0375	Aerial sRGB	8-Jun-09	96	0	4	0	99
DSC_0422	Aerial sRGB	8-Jun-09	88	0	11	0	98
DSC_0223	Aerial sRGB	10-Jun-09	46	1	53	0	93
DSC_0243	Aerial sRGB	10-Jun-09	59	1	40	1	98
DSC_0314	Aerial sRGB	10-Jun-09	89	0	11	0	95
DSC_0319	Aerial sRGB	10-Jun-09	75	2	19	4	88

DSC_0323	Aerial sRGB	10-Jun-09	37	2	61	0	95
DSC_0338	Aerial sRGB	10-Jun-09	83	2	15	1	95
DSC_0386	Aerial sRGB	10-Jun-09	80	3	14	3	89
DSC_0394	Aerial sRGB	10-Jun-09	79	2	10	9	95
DSC_0412	Aerial sRGB	10-Jun-09	63	2	24	10	92
DSC_0425	Aerial sRGB	10-Jun-09	56	2	17	24	97
DSC_0439	Aerial sRGB	10-Jun-09	71	1	6	22	98
DSC_0441	Aerial sRGB	10-Jun-09	57	0	4	38	98
DSC_0486	Aerial sRGB	10-Jun-09	53	1	17	29	96
DSC_0634	Aerial sRGB	10-Jun-09	72	1	14	12	96
DSC_0207	Aerial sRGB	13-Jun-09	80	1	19	0	96
DSC_0514	Aerial sRGB	13-Jun-09	86	1	13	0	97

1191 Results Table 2. The complete results of imagery processed for this analysis. Descriptions for each image includes the image
1192 type, date collected, the percent of the image that falls into each of the four categories, and the accuracy assessment.

1193

Image Source	Training Dataset Size	Out-of-bag Error
Panchromatic WorldView	1000	0.94
Pansharpened WorldView	859	0.89
Aerial Imagery	945	0.94
IceBridge Imagery	940	0.91

1194 Table 3. Out-of-Bag scores for the three training datasets used to classify imagery from each of the four sensor platforms
1195 and the number of objects manually classified for each set.

Deleted: .

Page 24: [1] Deleted **Nicholas C. Wright** **12/28/17 11:06:00 AM**

We next test the central limit theorem to see how well we can predict the error bounds from processing a single set of independent (i.e. randomly distributed) samples. The central limit theorem states that when taking the mean of a sufficiently large number of independent samples of a random variable, the standard error of the mean of the samples is equal to $\frac{\sigma}{\sqrt{N}}$ where σ is the standard deviation of the sample values and N is the sample size. The standard deviation of pond coverage fraction in sets of 100 sub-images ranged from 0.15 to 0.25 across the 1000 sample sets run (see histogram in Fig. 14b) This yields a predicted standard error of the mean determined from any one of these sets of 0.015 to 0.025. The observed standard deviation in the mean values across all 1000 sample sets presented in Fig. 14a is 0.0201, indicating that the central limit theorem applies in this case.

Returning

Page 24: [2] Deleted **Nicholas C. Wright** **12/28/17 11:06:00 AM**

, this time representing twice the standard error determined from the central limit theorem.

Page 24: [3] Deleted **Nicholas C. Wright** **12/28/17 11:06:00 AM**

permits expedient determination of melt pond fraction within that image area with small error bounds. If the total image is large enough, the value will be representative of the

Page 24: [4] Deleted **Nicholas C. Wright** **12/28/17 11:06:00 AM**

scale. In this case, processing as little as 5km^2 (~0.5%) of the image permits determination of a mean that lies within 0.025 of the true image mean 95% of the time. Also indicated on the plot is a 5% uncertainty band around the mean

Page 24: [5] Deleted **Nicholas C. Wright** **12/28/17 11:06:00 AM**

A test of the central value theorem again shows that it also applies in this case and provides a good estimate of the error of a mean ice fraction calculated from a set of random sub images. The green dots again indicate

Page 24: [6] Deleted **Nicholas C. Wright** **12/28/17 11:06:00 AM**

must process imagery representing at least 5km^2 in surface area, selected in at least

Page 32: [7] Deleted **Nicholas C. Wright** **12/28/17 11:06:00 AM**

Important

Page 32: [7] Deleted **Nicholas C. Wright** **12/28/17 11:06:00 AM**

Important

Page 32: [7] Deleted **Nicholas C. Wright** **12/28/17 11:06:00 AM**

Important

Page 32: [7] Deleted **Nicholas C. Wright** **12/28/17 11:06:00 AM**

Important

Page 32: [7] Deleted **Nicholas C. Wright** **12/28/17 11:06:00 AM**

Important

